Received: 1 December 2021 | Revised: 25 February 2022 | Accepted: 25 February 2022

DOI: 10.1002/wcms.1614

ADVANCED REVIEW

WIREs COMPUTATIONAL MOLECULAR SCIENCE WILEY

Time-dependent density matrix renormalization group method for quantum dynamics in complex systems

Jiajun Ren | **Weitang Li** | **Tong Jiang** | **Yuanheng Wang** | **Zhigang Shuai**

MOE Key Laboratory of Organic OptoElectronics and Molecular Engineering, Department of Chemistry, Tsinghua University, Beijing, People's Republic of China

Correspondence
Zhigang Shuai and Jiajun Ren, MOE Key Laboratory of Organic OptoElectronics and Molecular Engineering, Department of Chemistry, Tsinghua University, Beijing 100084, People's Republic of China.
Email: zgshuai@tsinghua.edu.cn and jiajunren0522@gmail.com

Funding information
Ministry of Science and Technology of China, Grant/Award Number: 2017YFA0204501; National Natural Science Foundation of China, Grant/Award Numbers: 21788102, 22003029

Edited by: Jinlong Yang, Associate Editor

Abstract

The simulations of spectroscopy and quantum dynamics are of vital importance to the understanding of the electronic processes in complex systems, including the radiative/radiationless electronic relaxation relevant for optical emission, charge/energy transfer in molecular aggregates related to carrier mobility in organic materials, as well as photovoltaic and thermoelectric conversion, light-harvesting and spin transport, and so forth. In recent years, time-dependent density matrix renormalization group (TD-DMRG) has emerged as a general, numerically accurate and efficient method for high-dimensional full-quantum dynamics. This review will cover the fundamental algorithms of TD-DMRG in the modern framework of matrix product states (MPS) and matrix product operators (MPO), including the basic algebra with respect to MPS and MPO, the novel time evolution schemes to propagate MPS, and the automated MPO construction algorithm to encode generic Hamiltonian. Most importantly, the proposed method can handle the mixed state density matrix at finite temperature, enabling quantum statistical description for molecular aggregates. We demonstrate the performance of TD-DMRG by benchmarking with the current state-of-the-art methods for simulating quantum dynamics of the spin-boson model and the Frenkel–Holstein(–Peierls) model. As applications of TD-DMRG to real-world problems, we present theoretical investigations of carrier mobility and spectral function of rubrene crystal, and the radiationless decay rate of azulene with an anharmonic potential energy surface.

This article is categorized under:
Theoretical and Physical Chemistry > Statistical Mechanics
Theoretical and Physical Chemistry > Reaction Dynamics and Kinetics
Software > Simulation Methods

KEYWORDS
density matrix renormalization group, matrix product operator, matrix product state, quantum dynamics

1 | INTRODUCTION

The (nonequilibrium) electronic dynamical processes in organic conjugated molecules, molecular aggregates, and molecular solids have been attracting great attention because these are essential to understanding the macroscopic phenomena and properties of complex molecular systems. For example, the efficient electronic excitation energy transfer (EET) process in the light-harvesting complexes is key to efficient natural photosynthesis[1,2]; the electron–hole separation/recombination and charge transport are key to the optoelectronic performances of organic semiconductors.[3–5] In addition to the electronic structure, the electronic dynamical processes in these complex systems are greatly influenced by the electron–vibration coupling (or electron–phonon coupling) because the carbon skeleton of organic polymers and molecules is quite flexible.[6] A large number of vibrational degrees of freedom (DoFs), including both the intramolecular vibrations and intermolecular vibrations, would not only dissipate the electronic energy but also modulate the nature of electronic states, such as the coherence to incoherence and the localization to delocalization transitions in molecular/polymeric aggregate with typical weak intermolecular interaction.[7,8] Time-dependent approaches are in general preferred for the computational investigation of electronic dynamical processes. First, these are able to provide the frequency-dependent dynamical properties in the framework of response theory, which can be directly compared with the spectroscopy experiments.[9] Moreover, these can also reveal the detailed real-time nonequilibrium dynamics, which can only be tracked with very limited spatial and temporal resolutions in experiments.

The computational challenges to simulate the dynamics lie in that these systems are essentially many-body systems and an exact solution of the time-dependent Schrödinger equation (TDSE) becomes unfeasible as a result of the so-called quantum exponential wall, that is, the dimension of the Hilbert space expands exponentially with the system size. Although a lot of useful approximate methods have been proposed in the last several decades,[10–15] the development of numerically exact full-quantum methods is still needed ("numerically exact" means that the accuracy can be systematically improved to approach the exact limit), because first these can be universally applicable to vibrational, vibronic, or electronic many-body problems and take the quantum effect fully into account; second, these can provide a reliable reference for approximate methods which can be safely used in large systems only after careful assessments. The early numerically exact wavepacket propagation methods include the split-operator Fourier transform (SOFT) method,[16] short iterative Lanczos method,[17] and Chebyshev polynomial expansion method.[18] These are successfully used for problems with a few DoFs, but are limited by exponential scaling. For high-dimensional problems, the best-known numerically exact wavefunction-based full-quantum dynamics methods are the multiconfiguration time-dependent Hartree method (MCTDH)[19] and its multilayer extension (ML-MCTDH),[20] which are quite universal for both dynamics of molecular systems in the gas phase and open quantum systems in the condensed phase.[21–23] ML-MCTDH can indeed lower the computational scaling and break the exponential wall. For open quantum systems, there are more numerically exact methods based on the reduced dynamics methodology, including the hierarchical equations of motion (HEOM),[24–27] quasi-adiabatic propagator path-integral (QUAPI),[28,29] non-Markovian quantum state diffusion (NMQSD),[30,31] and generalized quantum master equation,[32,33] and so forth.

Time-dependent density matrix renormalization group (TD-DMRG) is a wavefunction-based numerically exact full-quantum dynamics method.[34] DMRG was originally proposed by White in 1992, which successfully solved the ground state and several lowest excited states of one-dimensional (1-D) strongly correlated lattice models, such as Hubbard model and Heisenberg model.[35,36] Then, DMRG was quickly introduced into quantum chemistry by Shuai et al.[37] and Fano et al.[38] for the semi-empirical Pariser–Parr–Pople model and by White and Martin for ab initio Hamiltonian.[39] Now, it has become the state-of-the-art electronic structure method to handle multiconfigurational problems with strong electron correlation.[40] Recently, DMRG has quickly emerged as an efficient and accurate approach to solve the eigenvalue problem of nuclear SE to calculate the molecular vibrational structure and infrared spectrum.[41–44] The first successful time-dependent theory of DMRG started with the development of the time-evolving block decimation (TEBD) method proposed by Vidal, inspired by quantum information and quantum computation theory.[45] It is based on Trotter splitting of the formal propagator, which is most efficient for Hamiltonian with only 1-D nearest-neighbor interactions, otherwise, additional swap gates are needed.[46] Soon after, TEBD was reformulated into the language of traditional DMRG, named adaptive TD-DMRG.[47,48] Thanks to the discovery that the wavefunction ansatz of DMRG is a matrix product state (MPS),[49] the modern (TD-)DMRG has a very rigorous mathematical foundation.[50] In addition to MPS, another indispensable ingredient of modern DMRG is matrix product operator (MPO), which is a factorization of operators with respect to each DoF into a chain structure.[51] Several efficient methods have been proposed to encode a generic operator as an MPO.[44,52–54] This MPS/MPO formulation of (TD-)DMRG not only enriches the original theory but also brings about great conveniences for the implementation of (TD-)DMRG algorithms, and thus becomes more

and more popular nowadays. To handle Hamiltonian with arbitrary long-range interactions, a number of time evolution algorithms have been proposed. The two most popular methods are the global propagation-and-compression (P&C) methods[55–59] and the methods based on the time-dependent variational principle (TDVP).[60–64] MPS is actually a special type of tensor network state (TNS) with 1-D structure, which opens the door to the development of more general TNS, such as various flavors of tree tensor network states (TTNS),[65,66] projected entangled pair states (PEPS),[67] and so on. Some of these have already been used to solve the eigenvalue problem and dynamics of nuclear SE.[68] In addition to the rapid development of TD-DMRG algorithms,[69] the application scope of TD-DMRG is becoming more and more widespread. For quantum dynamics in the condensed phase, TD-DMRG has been used to study the dynamics of spin-boson model (SBM),[70] the exciton/charge transfer[64,71–75] and linear/nonlinear spectroscopy in natural and artificial molecular aggregates,[59,76] carrier transport mobility in molecular solids,[77,78] singlet fission,[79,80] and so on. For molecular dynamics in the gas phase, TD-DMRG has been used to study the ultrafast interconversion dynamics of pyrazine described by more general vibronic models,[58,63,80] and radiationless decay rate of azulene including the anharmonic effect.[81,82] In addition to the electron–vibration coupled problems, TD-DMRG has also been used to study the attosecond electron dynamics with ab initio electronic Hamiltonian, including the photoelectron spectrum of hydrogen chain and ultrafast charge migration in iodoacetylene and benzene.[83–85] Through treating these different problems, the accuracy, efficiency, and robustness of TD-DMRG have been well demonstrated by comparing to the other established numerically exact methods. Because (TD-)DMRG is quite general to efficiently handle high-dimensional problems, in most recent years, many established numerical methods have also been combined with the TD-DMRG algorithms, which greatly improves the capabilities to handle much larger systems and at the same time to keep high accuracy. The representative works include HEOM-MPS proposed by Shi et al.,[86] NMQSD + MPS proposed by Daley and coworkers,[87] time-evolving matrix product operator (QUAPI + MPO) proposed by Lovett and coworkers.[88] In turn, these cross-cutting methods also open up new opportunities for TD-DMRG.

The rest of this paper is structured as follows. In Section 2, we will describe the fundamental aspects of the modern TD-DMRG theory. We will first introduce the mathematical structure and physical interpretation of MPS and then move to the tangent space of MPS, which is key to a set of post-DMRG and time evolution algorithms. Second, we will introduce MPO, the other main ingredient in the modern TD-DMRG theory, and then describe how to construct a compact MPO from a generic operator. With MPS and MPO, the basic tensor algebra in DMRG is described in the graphic representation. Third, two types of time evolution algorithms to propagate a pure wavefunction are presented. Furthermore, how to handle mixed states and consider the temperature effect are discussed. Finally, a number of issues are discussed including the multiset method, ordering problem, the extension of MPS to more complicated TNS, and the CPU-GPU heterogeneous algorithm to accelerate computations. In Section 3, TD-DMRG is benchmarked against the state-of-the-art numerically exact methods to show its performance, including the spin dynamics in SBM and energy transfer in the Fenna–Matthews–Olson (FMO) complexes. In these examples, the key features of TD-DMRG are covered. In Section 4, two selected real applications are described. One is the calculation of charge carrier mobility and spectral function of rubrene crystal which is affected by both intramolecular and intermolecular vibrations. The other is the calculation of the radiationless decay rate of azulene including the anharmonic effect. In the last section, the conclusion and outlook are given.

2 | METHODOLOGY AND ALGORITHM

2.1 | Matrix product states

The matrix product state, as the name implies, is a wavefunction ansatz parameterized as the product of a sequence of matrices, which is later also called a tensor train format by mathematicians.[89] MPS is actually a low-rank approximation to the high-rank coefficient tensor of the exact multiconfigurational wavefunction.[50] For a system of N DoFs, MPS is written as

$$|\Psi\rangle = \sum_{\{\sigma\}} C_{\sigma_1\sigma_2\cdots\sigma_N} |\sigma_1\sigma_2\cdots\sigma_N\rangle, \tag{1}$$

$$\simeq \sum_{\{\sigma\},\{a\}} A[1]^{\sigma_1}_{a_1} A[2]^{\sigma_2}_{a_1 a_2} \cdots A[N]^{\sigma_N}_{a_{N-1}} \, |\, \sigma_1\sigma_2\cdots\sigma_N\rangle, \tag{2}$$

or abbreviated as $|\Psi\rangle = A[1]A[2]\cdots A[N]$. $\{a\}$, $\{\sigma\}$ represents the contraction over indices which appear more than once. $A[i]^{\sigma_i}_{a_{i-1}a_i}$ is the local matrix (more precisely, a rank-3 tensor) for the ith DoF, which has one physical index σ_i and two virtual indices (or virtual bonds) a_{i-1}, a_i ($a_0 = a_N = 1$ is conventionally omitted in Equation (2)). For nuclear motion problems, N is the number of modes. The physical index σ_i labels the primitive basis function $|\sigma_i\rangle$ for the ith mode, for example, the discrete variable representation (DVR) basis and simple harmonic oscillator (SHO) basis,[21,90] which is assumed to be orthonormal in this review. The size of the primitive basis function is denoted as d_i. For indistinguishable systems, to consider the exchange symmetry, DMRG can also be formulated in second quantization, in which N is the number of orbitals and $|\sigma_i\rangle$ stands for the occupation number in the Fock space.[36,50] The virtual index a_i connects two neighboring matrices, the size of which is called the bond dimension, denoted as $M_{S,i}$. The algebraic expression in DMRG is usually tedious, and thus it is more convenient to represent it graphically. As shown in Figure 1a, each rank-3 tensor is denoted as a 3-legged circle and the connected bond indicates that the corresponding index is contracted.

Because of the 1-D structure, MPS can be divided into the left- (L-) block and right- (R-) block after cutting one virtual bond. Following the philosophy of renormalization group, the renormalized states of DMRG for each block can be defined as

$$|\, a_i[1:i]\rangle = \sum_{\{a\},\{\sigma\}} A[1]^{\sigma_1}_{a_1} A[2]^{\sigma_2}_{a_1 a_2} \cdots A[i]^{\sigma_i}_{a_{i-1}a_i} \,|\, \sigma_1 \cdots \sigma_i\rangle, \tag{3}$$

$$|\, a_j[j+1:N]\rangle = \sum_{\{a\},\{\sigma\}} A[j+1]^{\sigma_{j+1}}_{a_j a_{j+1}} \cdots A[N]^{\sigma_N}_{a_{N-1}} \,|\, \sigma_{j+1} \cdots \sigma_N\rangle, \tag{4}$$

where [1:i] ([$j+1$:N]) indicates that the block is from the first to the ith DoF (from the last to the $(j+1)$th DoF). The renormalized states are the linear combination of the direct product basis after applying a series of rotation matrices $A[i]$ sequentially. In the ground state DMRG, the renormalized states are optimized for a single state.[36] In TD-DMRG, the renormalized states are time-dependent, optimized for the time-dependent wavefunction.[91] One local matrix, $A[n]^{\sigma_n}_{a_{n-1}a_n}$, can be regarded as the coefficient matrix in the renormalized space spanned by $|a_{n-1}[1:n-1]\rangle \bigotimes |\sigma_n\rangle \bigotimes |a_n[n+1:N]\rangle$. Note that, in general, the renormalized states are not necessary to be orthonormal. The overlap matrix between the renormalized states is $S[1:i]_{a_i a_i'} = \langle a_i[1:i]|a_i'[1:i]\rangle$, $S[j+1:N]_{a_j a_j'} = \langle a_j[j+1:N]|a_j'[j+1:N]\rangle$. Fortunately, the parameterization of MPS ansatz is redundant in that inserting $I = GG^{-1}$ (G is any invertible matrix with size $a_i \times a_i$) into the adjacent matrices will obtain the same wavefunction but with different local matrices $\cdots A'[i]A'[i+1]\cdots = \cdots(A[i]G)(G^{-1}A[i+1])\cdots = \cdots A[i]A[i+1]\cdots$. Taking advantage of this redundancy, it is convenient to define the canonical forms of an MPS, $|\Psi\rangle = L[1]L[2]\cdots L[n-1]C[n]R[n+1]\cdots R[N]$, in which

$$\sum_{\sigma_i, l_{i-1}} L[i]^{\sigma_i *}_{l_{i-1} l_i'} L[i]^{\sigma_i}_{l_{i-1} l_i} = \delta_{l_i' l_i}, \tag{5}$$

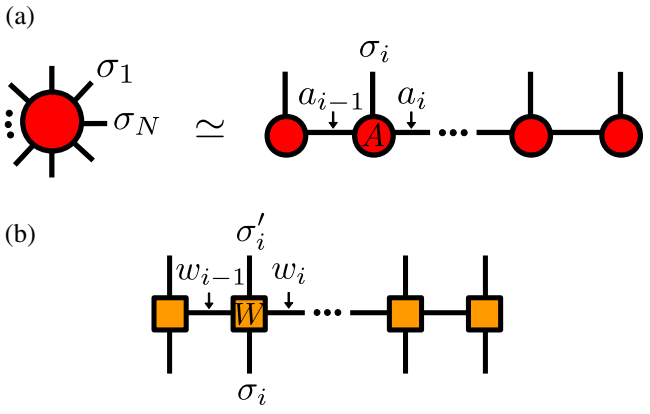

FIGURE 1 The graphic representation of (a) MPS (b) MPO

$$\sum_{\sigma_j, r_j} R[j]^{\sigma_j *}_{r'_{j-1} r_j} R[j]^{\sigma_j}_{r_{j-1} r_j} = \delta_{r'_{j-1} r_{j-1}}. \tag{6}$$

With Equations (5) and (6), the new renormalized states fulfill the orthonormal relation $S[1:i]_{l_i l'_i} = \delta_{l_i l'_i}$ ($i = 1, 2, ..., n-1$) and $S[j+1:N]_{r_j r'_j} = \delta_{r_j r'_j}$ ($j = n, n+1, ..., N-1$). The graphic representation is shown in Figure 2, in which the direction of the triangles denotes the canonical direction. When the canonical center $n = N$ ($n = 1$), it is called a left-(right-) canonical form, otherwise, it is called a mixed-canonical form. If $C[n]$ in the mixed-canonical form is further decomposed by QR decomposition

$$C[n]^{\sigma_n}_{l_{n-1} r_n} \overset{\text{reshape}}{\rightarrow} C[n]_{\sigma_n l_{n-1}, r_n} \overset{\text{QR}}{=} \sum_{l_n} L[n]_{\sigma_n l_{n-1}, l_n} D[n]_{l_n, r_n} \overset{\text{reshape}}{\rightarrow} \sum_{l_n} L[n]^{\sigma_n}_{l_{n-1} l_n} D[n]_{l_n r_n}, \tag{7}$$

$L[n]$ fulfills the relation in Equation (5). Afterwards, $D[n]$ is combined with $R[n+1]$ to obtain $C[n+1]^{\sigma_{n+1}}_{l_n r_{n+1}} = \sum_{r_n} D[n]_{l_n r_n} R[n+1]^{\sigma_{n+1}}_{r_n r_{n+1}}$ and apparently the canonical center is moved one site to the right. The reverse process to move the canonical center to the left can be carried out in a similar way as Equation (7) while QR is replaced with RQ decomposition. More generally, starting from any MPS, a canonical MPS with canonical center at n can be prepared by performing QR decomposition from site 1 to $n-1$ sequentially and RQ decomposition from the site N to $n+1$ sequentially, which is called *canonicalization*.

The MPS ansatz can be exact only when $M_{S,i}$ is allowed to exponentially increase with i until $N/2$ otherwise it is an approximation. In the other limit, if $M_{S,i} \equiv 1$, MPS is reduced to a Hartree product state, which treats the correlation between different DoFs at the mean-field level. In practice, the accuracy of an MPS can be systematically improved to achieve the numerically exact results by increasing the bond dimension $M_{S,i}$ only. Compared to the exact parameterization with d^N parameters in Equation (1), the number of parameters of an MPS is only $\mathcal{O}(NdM_S^2)$ (assuming $d_i \equiv d$, $M_{S,i} \equiv M_S$ for simplicity). If M_S only increases polynomially with respect to the system size N, MPS can in principle break the quantum exponential wall. The actual required $M_{S,i}$ is determined by the entanglement between the L- and R-blocks at each boundary. This entanglement can be characterized by the von Neumann entropy

$$S_{L/R} = -\mathrm{Tr}(\rho \log \rho) = -\sum_s \lambda_s \log \lambda_s. \tag{8}$$

ρ is the reduced density matrix of either L-block or R-block. λ_s is the eigenvalues of ρ. For a normalized wavefunction, $\mathrm{Tr}(\rho) = \sum_s \lambda_s = 1$. The L-block and R-block reduced density matrix of an MPS at the boundary between the nth and $(n+1)$th sites is $\rho_L[1:n] = D[n]D[n]^\dagger = \sum_{\sigma_n} C[n]^{\sigma_n} C[n]^{\sigma_n \dagger}$ and $\rho_R[n+1:N] = D[n]^\dagger D[n] = \sum_{\sigma_n} C[n]^{\sigma_n \dagger} C[n]^{\sigma_n}$, respectively. The minimum entropy is 0, which means the two blocks are not entangled ($\lambda_1 = 1, \lambda_{s \neq 1} \equiv 0$). The maximum entropy that can be captured is $\log M_{S,n}$, when the two blocks are maximally entangled ($\lambda_s \equiv 1/M_{S,n}$). Therefore, MPS is most efficient to represent states of low entanglement. In some special cases, such as the ground state of a gapped system with only nearest-neighbor interaction, the entanglement of the two blocks is only proportional to the area of the boundary, known as

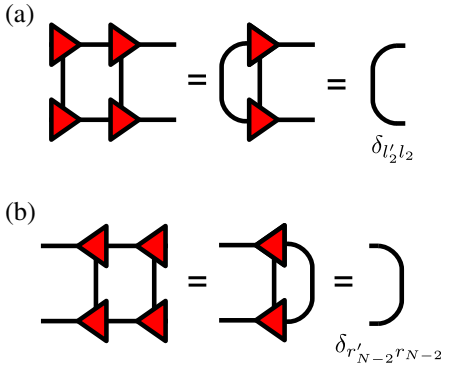

FIGURE 2 The (a) left-canonical (b) right-canonical condition (Equations (5) and (6)) of renormalized states. For simplicity, each block contains two sites

the area law.[92] In this case, if the system is 1-D, M_S is thus independent of the system size N. However, for time-dependent problems, the exact relationship of M_S with N and time t is still not clear except for a very few systems.[93,94] In spite of this, as it is believed that the real physical systems are of finite entanglement, MPS with a finite M_S can still represent the wavefunctions of real systems quite efficiently.

The spectrum of the reduced density matrix ρ can also be used to compress an MPS. If the QR decomposition in Equation (7) is replaced with singular value decomposition (SVD),

$$\begin{aligned} C[n]^{\sigma_n}_{l_{n-1}r_n} &\overset{\text{reshape}}{\rightarrow} C[n]_{\sigma_n l_{n-1},r_n} \overset{\text{SVD}}{=} \sum_{s=1}^{k} U[n]_{\sigma_n l_{n-1},s}\Gamma[n]_{ss}V[n]^{\dagger}_{s,r_n} \\ &\overset{\text{reshape}}{\rightarrow} \sum_{s=1}^{k} U[n]^{\sigma_n}_{l_{n-1}s}\Gamma[n]_{ss}V[n]^{\dagger}_{sr_n} \approx \sum_{l_n=1}^{\widetilde{M}_{S,n}<k} L[n]^{\sigma_n}_{l_{n-1}l_n}\Gamma[n]_{l_n l_n}V[n]^{\dagger}_{l_n r_n}, \end{aligned} \tag{9}$$

$\Gamma[n]$ is a real and nonnegative diagonal matrix with dimension $k = \min[d_n M_{S,n-1}, M_{S,n}]$. It is easy to check that $\Gamma[n]^2_{ss} = \lambda[n]_s$ if $\Gamma[n]_{ss}$ and $\lambda[n]_s$ in Equation (8) are both in descending order. $U[n]$ fulfills the relation in Equation (5). If only the largest $\widetilde{M}_{S,n}$ terms ($\widetilde{M}_{S,n} < k$) are retained, $\widetilde{C}[n]$ is a good approximation to $C[n]$ with a smaller bond dimension. The truncation error can be estimated by $\epsilon = 1 - \sum_{s=\widetilde{M}_{S,n}+1}^{k} \Gamma[n]^2_{ss}$ if $|\Psi\rangle$ is normalized. With this algorithm, an L(R)-canonical MPS $|\Psi\rangle$ could be compressed to $|\widetilde{\Psi}\rangle$ by successive approximate SVD decompositions from site N to 1 (site 1 to N). At each local step of the compression, two truncation criteria are commonly used[50] (i) a fixed pre-defined $\widetilde{M}_S$; (ii) adaptive $\widetilde{M}_S$ with all Γ_{ss} larger than pre-defined ζ retained. It is important to emphasize that the SVD compression of the coefficient matrix $C[n]$ is only valid when n is the canonical center. As the sweeping procedure of the SVD compression above is a greedy algorithm, $|\widetilde{\Psi}\rangle$ may not be the best approximation with a given M_S to $|\Psi\rangle$. The variational algorithm, which minimizes $\mathscr{L} = \left\| |\Psi\rangle - |\widetilde{\Psi}\rangle \right\|^2$ in a manner similar to the DMRG ground state optimization algorithm, is also widely used.[50] The $|\widetilde{\Psi}\rangle$ obtained by SVD compression can be used as the initial guess of the variational algorithm.

With MPS, the inner product of two wavefunctions $\langle\Phi|\Psi\rangle$ can be calculated conveniently, which is the full contraction of the tensor network in Figure 3a (since there is no dangling bond, the result is a scalar as expected). The key to efficiently contracting a tensor network is to find a contraction order which gives the lowest computational scaling. For the inner product, the best way is to sequentially contract two local matrices of the same site one by one, which gives the overall scaling $\mathcal{O}(NM_S^3 d)$. In addition to the inner product, the addition of two MPSs $|\chi(\mathbf{A}')\rangle = |\Psi(\mathbf{A})\rangle + |\Phi(\mathbf{B})\rangle$ is conveniently constructed by stacking the local matrices $[A[i], B[i]]$ block-diagonally except the first and the last sites. The graphic representation is shown in Figure 3b.

$$A'[1] = [A[1]\ B[1]],\quad A'[i] = \begin{bmatrix} A[i] & \mathbf{0} \\ \mathbf{0} & B[i] \end{bmatrix}\ (i = 2,3,...,N-1),\quad A'[N] = \begin{bmatrix} A[N] \\ B[N] \end{bmatrix}. \tag{10}$$

2.2 | Tangent space of MPS

The tangent space of MPS is an essential concept in the development of MPS theories for excitations, spectral functions, and time evolutions based on TDVP both for periodic systems and finite systems.[60,62,95–98] The tangent space of a given

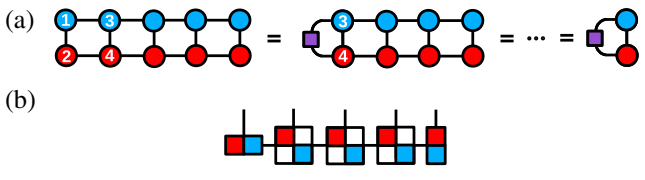

FIGURE 3 (a) The tensor network to calculate $\langle\Phi|\Psi\rangle$. The order of contraction which gives the lowest computational scaling follows 1, 2, 3, 4, ... (b) The block diagonal structure of $|\chi(\mathbf{A}')\rangle = |\Psi(\mathbf{A})\rangle + |\Phi(\mathbf{B})\rangle$. For simplicity, $N = 5$

MPS is spanned by the partial derivatives with respect to all the local matrices. Any vector in the first order tangent space can be written as

$$|\Psi_T(\mathbf{B})\rangle = \sum_i \sum_{\sigma_i a_{i-1} a_i} B[i]^{\sigma_i}_{a_{i-1}a_i} \,|\, a_{i-1}[1:i-1]\rangle \,|\, \sigma_i\rangle \,|\, a_i[i+1:N]\rangle. \tag{11}$$

However, there are two problems with the tangent space bases $|a_{i-1}[1{:}i-1]\rangle|\sigma_i\rangle|a_i[i+1{:}N]\rangle$. First, the bases are not orthonormal to each other for a general MPS, which is not convenient to use. Second, because of the redundancy of MPS parameterization, the bases are linearly dependent, for example, when $B[i] = X[i-1]A[i] - A[i]X[i]$ ($X[i]$ is of size $a_i \times a_i$ and $X[0] = X[N] = 1$), $|\Psi_T(\mathbf{B})\rangle = 0$. To solve these two problems, there is no unique prescription. One smart choice is that the bases of tangent space are defined with respect to multiple mixed-canonical forms of the same MPS with the canonical centers iterating through all the sites.[62] Under this condition, the bases belonging to one single canonical center are orthonormal $\left\langle l'_{i-1}\sigma'_i r'_i | l_{i-1}\sigma_i r_i \right\rangle = \delta_{l_{i-1}l'_{i-1}}\delta_{\sigma_i\sigma'_i}\delta_{r_i r'_i}$. Additionally, to eliminate the linear dependency, $B[i]$ should satisfy a constraint, which is the left-orthonormal constraint $\sum_{\sigma_i l_{i-1}} B[i]^{\sigma_i}_{l_{i-1}r_i} L[i]^{\sigma_i *}_{l_{i-1}l_i} = 0$ for $i < n$ and the right-orthonormal constraint $\sum_{\sigma_i r_i} B[i]^{\sigma_i}_{l_{i-1}r_i} R[i]^{\sigma_i *}_{r_{i-1}r_i} = 0$ for $i > n$ (n can be any index from 1 to N). This constraint also ensures the bases belonging to different canonical centers to be orthonormal to each other. Without loss of generality, we choose $n = N$ here and thus only the left-orthonormal constraint is imposed. If $\overline{L}[i]_{l_{i-1}\sigma_i,\bar{l}_i}$ is the complementary orthonormal space of $L[i]_{l_{i-1}\sigma_i,l_i}$ (the stack of the two matrices along the column gives a unitary matrix), the definition of $B[i]$ is

$$B[i]^{\sigma_i}_{l_{i-1}r_i} = \begin{cases} \sum_{\bar{l}_i} \overline{L}[i]_{l_{i-1}\sigma_i,\bar{l}_i} X[i]_{\bar{l}_i r_i} & \text{if } i < N \\ X[N]^{\sigma_N}_{l_{N-1}} & \text{if } i = N \end{cases}. \tag{12}$$

Therefore, the parameterization of any tangent space vector based on the independent parameters X is

$$|\Psi_T(\mathbf{X})\rangle = \sum_{i=1}^{N-1} \sum_{\bar{l}_i r_i} X[i]_{\bar{l}_i r_i} \,|\, \bar{l}_i[1:i]\rangle \,|\, r_i[i+1:N]\rangle + \sum_{l_{N-1}\sigma_N} X[N]^{\sigma_N}_{l_{N-1}} \,|\, l_{N-1}[1:N-1]\rangle \,|\, \sigma_N\rangle. \tag{13}$$

$$|\, \bar{l}_i[1:i]\rangle = \sum_{\sigma_i l_{i-1}} \overline{L}[i]_{l_{i-1}\sigma_i,\bar{l}_i} \,|\, \sigma_i\rangle \,|\, l_{i-1}[1:i-1]\rangle. \tag{14}$$

With these orthonormal tangent space bases, the analytical linear response theory can be derived on top of the ground state MPS to calculate the excited states and spectral functions.[96–98] For time evolution schemes based on TDVP, the tangent space projector is necessary, which projects any state onto the tangent space of an MPS. According to the above smart parameterization of tangent space vectors, no matter what n is, the projector is the same, which is defined as

$$\widehat{P} = \sum_{i=1}^{N} \widehat{P}[1:i-1] \otimes \widehat{I}_i \bigotimes \widehat{P}[i+1:N] - \sum_{i=1}^{N-1} \widehat{P}[1:i] \bigotimes \widehat{P}[i+1:N], \tag{15}$$

where

$$\widehat{P}[1:i] = \sum_{l_i} |\, l_i[1:i]\rangle\langle l_i[1:i]\,|\,. \tag{16}$$

$$\widehat{P}[i+1:N] = \sum_{r_i} |r_i[i+1:N]\rangle\langle r_i[i+1:N]|. \tag{17}$$

$$\widehat{I}_i = \sum_{\sigma_i} |\sigma_i\rangle\langle\sigma_i|. \tag{18}$$

$$\widehat{P}[1:0] = \widehat{P}[N+1:N] = 1. \tag{19}$$

The graphic representation of this projector is shown in Figure 4. Combining the "+" and "−" terms with the same index i together in Equation (15) corresponds to projecting the $L[i]_{l_{i-1}\sigma_i,l_i}$ components out from the complete space to get the $\overline{L}[i]_{l_{i-1}\sigma_i,\bar{l}_i}$ components.[64,97]

Besides this type of parameterization based on multiple mixed-canonical forms, all the tangent space bases can be defined with respect to one single mixed-/left-/right-canonical MPS or even any general MPS. However, in these cases, in addition to the constraint on $B[i]$, the inverse of the overlap matrix $S[1{:}i]$ and $S[j{:}N]$ between the renormalized states should be explicitly calculated to orthogonalize the bases. The readers are referred to Reference 64 for the general expression of tangent space projector of any MPS. We will show below that the different definitions of tangent space projectors will lead to different flavors of TDVP-based time evolution schemes.

2.3 | Matrix product operators

Besides MPS, another ingredient of modern DMRG is the MPO, which is a factorization of an operator into the product of a chain of matrices.[51] The graphic representation is shown in Figure 1b.

$$\widehat{O} = \sum_{\{w\},\{\sigma\},\{\sigma'\}} W[1]^{\sigma_1',\sigma_1}_{w_1} W[2]^{\sigma_2',\sigma_2}_{w_1 w_2} \cdots W[N]^{\sigma_N',\sigma_N}_{w_{N-1}} \,|\, \sigma_1'\sigma_2'\cdots\sigma_N'\rangle\langle\sigma_N\sigma_{N-1}\cdots\sigma_1 \,|\,. \tag{20}$$

In principle, any operator can be factorized into an MPO by numerically decomposing the full-rank matrix representation of the operator sequentially. Similar to MPS, if the bond dimension $M_{\mathrm{O},i}$ is allowed to increase exponentially, this factorization can be exact. However, assuming that the size of the local primitive basis is $d = 10$, this numerical decomposition is not practically affordable if N exceeds 10. Fortunately, most operators of interest are of analytical sum-of-products (SOP) forms, such as all the model Hamiltonians encountered in Sections 3 and 4. In addition, in real problems, not all the DoFs have direct interactions (there are at most p-body interactions, or in other words, the interaction topology is very sparse), for example, there are at most two-body interactions in SBM (Section 3.1). With these two requirements, the bond dimension $M_{\mathrm{O},i}$ can be largely reduced. In SBM, although the number of interaction terms K in the Hamiltonian is $\mathcal{O}(N_b)$ (N_b is the number of bath DoFs), $M_{\mathrm{O},i}$ is a constant independent of N_b.[44] Generally speaking, the smaller p is, the smaller M_{O} is.

There are several advantages to introducing MPO. First, compared to the full matrix representation of a Hamiltonian, whose dimension is d^N, the MPO representation will not only significantly reduce the memory to store the Hamiltonian but also make some frequently encountered calculations related to operators, such as one operator acting on wavefunction $\widehat{O}\,|\Psi\rangle$ and the expectation value $\langle\Psi|\widehat{O}|\Psi\rangle$, much more efficient and convenient (graphically shown in Figure 5). In the calculation of expectation value of Hamiltonian and its derivative with respect to each local site (the most time-consuming part in TDVP-based time evolution schemes in Section 2.4.2), if each term of Hamiltonian is calculated independently, the computational scaling is $\mathcal{O}\big(K\big(NM_{\mathrm{S}}^3 d + M_{\mathrm{S}}^2 d^2\big)\big)$, which is proportional to the number of terms K. The introduction of MPO actually caches the matrix elements of operators for multiple usages during a single left-to-right sweep with scaling $\mathcal{O}\big(N\big(M_{\mathrm{O}}^2 M_{\mathrm{S}}^2 d^2 + M_{\mathrm{O}} M_{\mathrm{S}}^3 d\big)\big)$ if MPO is treated as dense matrices.[51,64] Hence, the computational cost could be largely reduced if K is large while M_{O} is small (see example in Section 3.1). In fact, the cache of

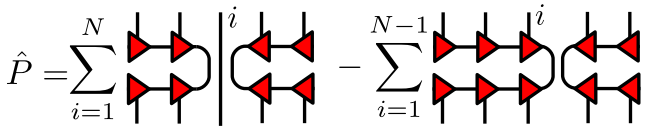

FIGURE 4 The graphic representation of tangent space projector of an MPS with respect to multiple mixed-canonical forms. For simplicity, $N = 5$

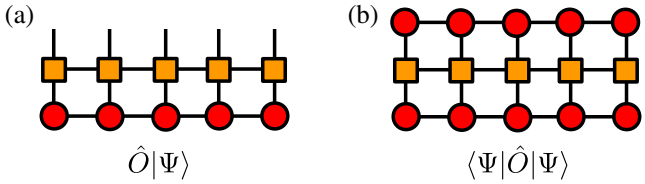

FIGURE 5 The graphic representation of (a) $\widehat{O}\,|\,\Psi\rangle$ and (b) $\langle\Psi|\widehat{O}|\Psi\rangle$

matrix elements of operators has already been considered in the traditional DMRG algorithms without MPO, which is called the renormalized operators—the matrix representation of operators in each block spanned by the renormalized states.[36,53] Moreover, when calculating the expectation value, the renormalized operator based algorithm has a lower scaling than the above analysis, which can only be obtained in the MPO-based algorithms by considering the sparsity of MPO.[52,53,99] From this aspect, MPO seems to have no advantage over the renormalized operator. However, the renormalized operators only approximate the exact operators $\widehat{O}$ as $\widehat{P}\widehat{O}\widehat{P}$, in which $\widehat{P}$ is the projector onto the renormalized space. Although there is no difference when calculating $\langle\Psi|\widehat{O}|\Psi\rangle$ because $|\,\Psi\rangle = \widehat{P}\,|\,\Psi\rangle$, MPO-based algorithm can calculate $\widehat{O}\,|\,\Psi\rangle$ (Figure 5a) and the second moment of Hamiltonian $\langle\Psi|\widehat{H}\widehat{H}|\Psi\rangle$ exactly, instead of the approximate $\widehat{P}\widehat{O}\,|\,\Psi\rangle$ and $\langle\Psi|\widehat{H}\widehat{P}\widehat{H}|\Psi\rangle$ by the renormalized operator based algorithm. $\widehat{O}\,|\,\Psi\rangle$ is key to the global P&C time evolution schemes in Section 2.4.1 and other DMRG algorithms relying on the global arithmetic.[100] The second moment of Hamiltonian is important to the calculation of spectral function by the dynamical DMRG method[83,101,102] or the estimation of the truncation error in calculating the ground state.[54,103] In addition to this, in the implementation based on renormalized operators, the necessary operators for a specific Hamiltonian are usually hard-coded, which is difficult to generalize to other Hamiltonian, although the DMRG ground state, excited states, and time evolution algorithms are universal. The introduction of MPO separates the definition of Hamiltonian from the following DMRG algorithms. Henceforth, one single DMRG code can in principle be universal enough to deal with a general Hamiltonian, which is provided by the users as an MPO. Furthermore, with the automated MPO construction algorithm introduced below, even a Hamiltonian written in a symbolic format can be used as input according to a friendly interface. This feature is particularly important to quantum dynamics because the electron-vibration coupled model Hamiltonian or the molecular nuclear Hamiltonian with different potential energy surfaces (PESs) are quite flexible.

Then, the question is how to construct the MPO for a generic operator. The MPO for the same operator could be completely different as long as the final product is correct. Since the cost of most DMRG algorithms increases polynomially with the MPO bond dimension M_{O}, it is preferred to construct an MPO as compact as possible, that is, with the smallest M_{O}, which is however nontrivial. Here, we focus on the operators of an analytical SOP form. The operators that do not have this form, especially molecular PES, will be discussed briefly at the end of this section. For simplicity, let us start with a system divided into the L- and R-block, and there is only one site in each block, which can include a single DoF or multiple DoFs. Without loss of generality, any operator can be written as

$$\widehat{O} = \sum_{i=1}^{I}\sum_{j=1}^{J}\gamma_{ij}\widehat{U}_i\widehat{V}_j, \quad \widehat{U}_i/\widehat{V}_j \in \text{L-/R-block}. \tag{21}$$

$\widehat{U}_i$ and $\widehat{V}_j$ are called the elementary operators and there is no redundancy in the operator sets $\left\{\widehat{U}_i\right\}$ and $\left\{\widehat{V}_j\right\}$. Note that $\widehat{U}_i$ and $\widehat{V}_j$ can be either first quantized operators or second quantized operators. The first naive two-site MPO with $M_{\mathrm{O}} = I \times J$ can be written as

$$\widehat{O} = \left[\widehat{U}_1,\ldots,\widehat{U}_1,\widehat{U}_2,\ldots,\widehat{U}_2,\ldots,\widehat{U}_I\ldots,\widehat{U}_I\right]\left[\gamma_{11}\widehat{V}_1,\ldots,\gamma_{1J}\widehat{V}_J,\gamma_{21}\widehat{V}_1,\ldots,\gamma_{2J}\widehat{V}_J,\ldots,\gamma_{I1}\widehat{V}_1,\ldots,\gamma_{IJ}\widehat{V}_J\right]^T. \tag{22}$$

In practice, because the interactions between the two sites are sparse, some γ_{ij} are probable to be zero, which can be eliminated to make the MPO more compact. Given that there are K terms with nonzero prefactor ($K \geq I$, $K \geq J$), M_{O} is K at maximum. Furthermore, this size of MPO can be reduced with the complementary operator technique,[104] which is essentially the factorization in elementary algebra. The complementary operators to $\widehat{U}_i$ in the R-block can be defined as $\widetilde{\widehat{V}}_i = \sum_j \gamma_{ij}\widehat{V}_j$. With this strategy, elementary operators are only retained in the L-block and the complementary operators are only retained in the R-block, which leads to $M_O = I$.

$$\widehat{O} = \left[\widehat{U}_1, \widehat{U}_2, ..., \widehat{U}_I\right] \left[\sum_j \gamma_{1j}\widehat{V}_j, \sum_j \gamma_{2j}\widehat{V}_j, ..., \sum_j \gamma_{Ij}\widehat{V}_j\right]^T. \quad (23)$$

If $J < I$, it is better to construct the complementary operators in the L-block in a similar manner, which gives $M_O = J$. Despite the improvement, these two strategies of complementary operators do not make use of the sparsity of γ_{ij}. By smartly constructing the complementary operators in both the L-block and the R-block according to the sparse interactions, it is possible to make the MPO more compact. Overall, M_O is equal to the total number of retained elementary operators and complementary operators in either block. One simple example is that when $\widehat{O} = \gamma_{11}\widehat{U}_1\widehat{V}_1 + \gamma_{12}\widehat{U}_1\widehat{V}_2 + \gamma_{23}\widehat{U}_2\widehat{V}_3 + \gamma_{33}\widehat{U}_3\widehat{V}_3$, the most compact MPO has $M_O = 2$ instead of 3, with $\widehat{O} = \widehat{U}_1\left(\gamma_{11}\widehat{V}_1 + \gamma_{12}\widehat{V}_2\right) + \left(\gamma_{23}\widehat{U}_2 + \gamma_{33}\widehat{U}_3\right)\widehat{V}_3$. For MPO of multiple sites, the problem becomes even more complicated, because the complementary operators at one boundary will affect the other boundaries and thus they should be designed in a global manner. The most common method is to design the complementary operators in a handcrafted way and then construct the MPO symbolically (or sometimes called analytically) by inspecting the recurrence relation between neighboring sites.[50,53] This method is most widely used for operators in which each site is of equal footings, such as the Heisenberg model,[50,51] the ab initio molecular electronic Hamiltonian,[53] and so on. The symbolic feature of this method can maintain the sparsity in MPO to reduce the computational cost in the DMRG algorithms. However, this method is not automated and the compactness of the MPO depends on the experience of the developer. The second method is a numerically "top-down" algorithm in which a naive MPO is first constructed by adding up the MPOs for each operator term together, each of which trivially has $M_O = 1$. Adding two MPOs is similar to adding two MPSs, shown in Figure 3b. After that, it is compressed by SVD or by removing the linearly dependent terms.[54] This algorithm is generic and automated for different operators, while a numerical error is introduced and additionally the time cost spent on the numerical compression is not negligible when the number of terms K is large. Besides the numerical compression method, Keller et al. proposed an automated and symbolic fork-merge method to improve the naive MPO by merging the identical subsequences among different terms,[52] which has been used in the construction of ab initio electronic Hamiltonian[52] and vibrational Hamiltonian.[42] Although the scaling of the MPO bond dimension with respect to the number of sites is correct, whether the obtained MPO is the most compact one is unclear.

Recently, we proposed a generic, automated, and symbolic algorithm based on the bipartite graph theory.[44] The obtained MPO has been proved to be the most compact one with respect to a given order of DoFs. The key idea of this algorithm is to represent the interactions between the L-block and R-block in Equation (21) as a bipartite graph $G = (U, V, E)$. The nonredundant operator set $U = \left\{\widehat{U}_i\right\}, V = \left\{\widehat{V}_j\right\}$ are represented as the vertices. The K interaction terms are represented as the edges denoted as E, each connecting one vertex in U to one vertex in V with a prefactor γ_{ij}. The sparsity of interactions is reflected in the fact that the bipartite graph is not fully connected. An example of mapping an operator to a bipartite graph is shown in Figure 6. If a vertex in the R-/L-block is picked, a complementary operator in the L-/R-block is constructed, which is the summation of the operators connected to this vertex after being multiplied by the prefactor of the corresponding edge. This pair of elementary and complementary operators is retained in the corresponding block respectively. Note that each edge should be only accounted for once to avoid double-counting. According to this rule, the minimum number of retained operators in one block that can include all the interactions is equal to the minimum number of vertices that can cover all the edges. The latter problem is the well-known minimum vertex cover problem in graph theory, which is to find the minimum set of vertices that includes at least one endpoint of every edge of the graph.[105] König theorem states that the minimum vertex cover in a bipartite graph is equal to the maximum matching problem (the maximum matching is the maximum edge set in which any two edges do not share one vertex), which can be solved by the Hungarian algorithm[106] or the Hopcroft–Karp algorithm[107] through finding an augmenting path.[105] In the example of Figure 6, the three red edges form a maximum matching, and the three blue vertices form a minimum vertex cover, indicating that the minimum MPO bond dimension is three. For a chain of multiple sites, a successive sweep from the left to the right (or right to left) is carried out. At each boundary, the optimal complementary operators are chosen according to the above bipartite graph-based algorithm. In the left-to-right sweeping case, U is composed of not only elementary operators but also complementary operators formed at the former boundaries. It has been further proved that this seeming greedy sweeping algorithm can give the most compact MPO when the order of the DoFs is already given. The details can be referred to Reference 44. The MPO obtained by this algorithm is an exact representation of the original Hamiltonian. If this exactness is not necessary, the MPO can be further numerically compressed to reduce the size.[53,82]

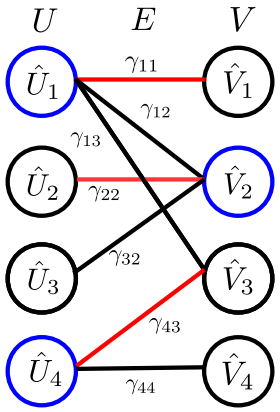

FIGURE 6 An example of mapping the operator $\hat{O}=\gamma_{11}\hat{U}_1\hat{V}_1+\gamma_{12}\hat{U}_1\hat{V}_2+\gamma_{13}\hat{U}_1\hat{V}_3+\gamma_{22}\hat{U}_2\hat{V}_2+\gamma_{32}\hat{U}_3\hat{V}_2+\gamma_{43}\hat{U}_4\hat{V}_3+\gamma_{44}\hat{U}_4\hat{V}_4$ to a bipartite graph $G=(U, V, E)$. The vertices represent the non-redundant operators in the left- and right-block. The edges represent the interactions with a nonzero prefactor. The blue vertices form a minimum vertex cover. The red edges form a maximum matching. According to the minimum vertex cover, the optimal complementary operators are $\widehat{\widetilde{V}}_1=\gamma_{11}\hat{V}_1+\gamma_{12}\hat{V}_2+\gamma_{13}\hat{V}_3$, $\widehat{\widetilde{U}}_2=\gamma_{22}\hat{U}_2+\gamma_{32}\hat{U}_3$, $\widehat{\widetilde{V}}_4=\gamma_{43}\hat{V}_3+\gamma_{44}\hat{V}_4$, which gives $M_O=3$ (reprinted with permission from Reference 44)

Before closing this section, we briefly discuss how to encode the molecular PES as MPO, which is crucial for the application of TD-DMRG in molecular quantum dynamics. A general molecular PES is a complex high-dimensional function without an analytical form. Hence, the above methods for operators of analytical SOP form cannot be used directly. If $N\sim 10$ and the PES is known at all direct product grids, the direct decomposition of the PES $V_{\sigma_1\cdots\sigma_N}$ by SVD can be performed to obtain a numerical SOP form, similar to decomposing the exact multiconfigurational wavefunction to an MPS. A cutoff ζ should be predetermined to truncate the bond dimension. The approximated $\tilde{V}_{\sigma_1\cdots\sigma_N}=\sum_{\{w\}}W^{\sigma_1}_{w_1}W^{\sigma_2}_{w_1w_2}\cdots W^{\sigma_N}_{w_{N-1}}$ can be further optimized by minimizing $\left\|\tilde{V}-V\right\|^2$. This numerical decomposition method is quite similar to the Potfit method,[108] which is widely used in MCTDH to transform a general PES on direct product grids into a Tucker format. The similar idea of multigrid Potfit can also be borrowed to MPS to allow a slightly larger N.[109] For N much larger than 10, how to transform a general PES into an SOP form is still an open question. Several methods have been proposed, including the single hidden layer neural network with exponential activation function (expNN),[110,111] the n-mode representation (n-MR)[112] combined with function fitting[113] or numerical decomposition,[114] and so on. However, expNN is limited by the expressive power of only one hidden layer. n-MR is limited by the number of terms that increase combinatorially with n.

2.4 | Time evolution algorithms

In TD-DMRG, the available time evolution schemes can be roughly classified into three groups. The first group is based on globally approximating the formal propagator $e^{-iH\tau}$ or $e^{-iH\tau}|\Psi\rangle$, including TEBD,[45,47,48] W$^{\mathrm{I,II}}$ method,[57] Runge–Kutta,[55,59] Chebyshev expansion,[115] Krylov subspace[55,56] methods, and SOFT method.[58] The same feature shared in these schemes is that in each time step the wavefunction is firstly propagated as a whole globally and then compressed to an affordable size in order to continue the propagation. We call these schemes the "global propagation and compression" scheme. The second group is based on TDVP.[116] Depending on the different ways to define the tangent space vectors, this group includes the original method with respect to a fixed canonical form[60] and the more recent projector-splitting algorithm (PS) with respect to multiple mixed-canonical forms.[62] The third group is more inspired by the traditional DMRG, which is formulated in the local renormalized space and the basis is adapted by the averaged reduced density matrix. The representatives are the time step targeting method[117] and some related variants.[83] Among the above evolution schemes, all schemes can be directly applied to models with long-range interactions except TEBD. For SBM with one spin or two spins, Pleino et al. developed the time-evolving density matrix with orthogonal polynomial algorithm, which unitary transforms the bath spectral density (BSD) to an effective 1-D chain with only nearest-neighbor

interaction and then can be efficiently simulated by TEBD.[70,118] Beyond this special case, the time evolution schemes for long-range interaction are more suitable. In this section, we introduce the P&C scheme combined with Runge–Kutta algorithm (P&C-RK) and the TDVP-based schemes in detail.

2.4.1 | Propagation and compression combined with the Runge–Kutta methods

Taking use of the arithmetic operations with MPS and MPO, the time-derivative $|\dot{\Psi}(t)\rangle = -i\widehat{H}(t)\,|\Psi(t)\rangle$ can be calculated directly, which gives another enlarged MPS. Further combined with a proper integrator for initial value problems (IVP), TDSE can be integrated. The simplest integrator is the explicit Euler method, $|\Psi(t+\tau)\rangle = |\Psi(t)\rangle - i\tau\widehat{H}(t)\,|\Psi(t)\rangle$, which only needs the current MPS and its time-derivative. How to add two MPSs is introduced in Section 2.1. In practice, high-order methods should be used to reduce the time-integration error, such as the explicit Runge–Kutta methods.[119] Since $\widehat{H}(t)\,|\Psi\rangle$ will give an MPS with bond dimension $M_{\mathrm{O}}M_{\mathrm{S}}$, and $|\Psi(\mathbf{A})\rangle + |\Phi(\mathbf{B})\rangle$ will give an MPS with bond dimension $M_{\mathrm{S},A} + M_{\mathrm{S},B}$, which in most cases is too large to keep the propagation going on. Therefore, the enlarged MPS should be compressed in P&C methods after each time step. The error of P&C-RK comes from two sources: the error of IVP integrator, which monotonically increases with the time step size; the error of MPS compression, which increases as the number of compressions increases or the bond dimension of MPS decreases. The advantage of P&C is that the bond dimension can be adaptively optimized in the time propagation by controlling the singular value cutoff ζ in the compression process. We found that $\zeta \leq 10^{-4}$ in most cases can already get a reasonably good result. With regard to the time step size, the error of P&C does not have a monotonic relationship with it if the cutoff ζ has been predetermined. The reason is that although a smaller time step size will improve the accuracy of the integrator, if the increment of the wavefunction after one time step is smaller than the truncation cutoff ζ, the increment is likely to be ruined after compression and then the overall accuracy deteriorates. Considering that the adaptive time-stepping algorithm is very important to propagate unknown systems, this drawback will make the implementation of an adaptive time-stepping algorithm in P&C, such as the embedded methods in Runge–Kutta families,[119] a bit difficult. One prescription is that the error control in the compression of MPS should be more strict than that in the adaptive time-stepping algorithm. Finally, the P&C method is most efficient for problems in which the MPO of Hamiltonian has a relatively small bond dimension M_{O}, otherwise, the canonicalization and compression by QR and SVD algorithms will be the bottleneck which is hard to accelerate by parallelization (see Section 3.2).

2.4.2 | TDVP algorithm

Another popular algorithm to propagate MPS is based on the Dirac–Frenkel TDVP $\langle\delta\Psi|i\partial/\partial t - \widehat{H}|\Psi\rangle = 0$.[116] TDVP provides a deterministic wavefunction path during the time evolution, which is locally optimal. The advantage of TDVP-based algorithms is that they can strictly conserve the norm of the wavefunction and the total energy in the real-time propagation with a time-independent Hamiltonian,[120] which is believed to be essential for long-time dynamics. The key ingredient of TDVP-based algorithms is the tangent space of MPS. In a geometric fashion, TDVP could be understood as a projection of the time-derivative $-i\widehat{H}\,|\Psi\rangle$ onto the tangent space of $|\Psi(t)\rangle$ at the current time $|\dot{\Psi}(t)\rangle = -i\widehat{P}\widehat{H}\,|\Psi(t)\rangle$ in order to constrain $|\Psi(t)\rangle$ to the MPS manifold. Two slightly different equations of motion (EOMs) are derived depending on the definition of tangent space vectors.

TDVP-VMF/CMF

One is based on the fixed canonical form (take left-canonical form $|\Psi\rangle = L[1]L[2]\cdots L[N-1]C[N]$ as an example),

$$i\frac{\partial C[N]^{\sigma'_N}_{l'_{N-1}}}{\partial t} = \sum_{\sigma''_N, l''_{N-1}} H[N]_{l'_{N-1}\sigma'_N, l''_{N-1}\sigma''_N} C[N]^{\sigma''_N}_{l''_{N-1}}, \tag{24}$$

$$i\frac{\partial L[i]^{\sigma'_i}_{l'_{i-1}l'_i}}{\partial t} = \sum_{l_{i-1},\sigma_i} \left(\delta_{l'_{i-1}l_{i-1}}\delta_{\sigma'_i\sigma_i} - p[i]_{l'_{i-1}\sigma'_i, l_{i-1}\sigma_i}\right) \sum_{l_i} S[i+1:N]^{-1}_{l'_i l_i} \sum_{l''_{i-1},\sigma''_i,l''_i} H[i]_{l_{i-1}\sigma_i l_i, l''_{i-1}\sigma''_i l''_i} L[i]^{\sigma''_i}_{l''_{i-1}l''_i}, \tag{25}$$

where

$$H[i]_{l'_{i-1}\sigma'_i l'_i, l_{i-1}\sigma_i l_i} = \sum_{\{w\}} h[1:i-1]_{\{l',w,l\}_{i-1}} W[i]^{\sigma'_i,\sigma_i}_{w_{i-1}w_i} h[i+1:N]_{\{l',w,l\}_i}. \tag{26}$$

$$h[1:i-1]_{\{l',w,l\}_{i-1}} = \sum_{\{l'\},\{w\},\{l\}} h[1]_{\{l',w,l\}_1} \cdots h[i-1]_{\{l',w,l\}_{i-2},\{l',w,l\}_{i-1}} \tag{27}$$

$$h[i+1:N]_{\{l',w,l\}_i} = \sum_{\{l'\},\{w\},\{l\}} h[i+1]_{\{l',w,l\}_i,\{l',w,l\}_{i+1}} \cdots h[N]_{\{l',w,l\}_{N-1}}. \tag{28}$$

$$h[i]_{\{l',w,l\}_{i-1},\{l',w,l\}_i} = \sum_{\sigma_i,\sigma'_i} A[i]^{\sigma'_i *}_{l'_{i-1}l'_i} W[i]^{\sigma'_i,\sigma_i}_{w_{i-1}w_i} A[i]^{\sigma_i}_{l_{i-1}l_i} \quad (A = L \text{ or } C). \tag{29}$$

$$p[i]_{l'_{i-1}\sigma'_i, l_{i-1}\sigma_i} = \sum_{l_i} L[i]^{\sigma'_i}_{l'_{i-1}l_i} L[i]^{\sigma_i *}_{l_{i-1}l_i}. \tag{30}$$

These coupled nonlinear equations closely resemble the EOMs of (ML-)MCTDH.[21] In Section 2.7, we will discuss the relation between TD-DMRG and (ML-)MCTDH. These equations can be solved by a proper IVP integrator, which is called the variable mean field algorithm (VMF) following the convention in MCTDH. With VMF, the MPS is globally updated after a single time step. The second-order approximation to it called constant mean field (CMF) can also be adopted,[64] in which $H[i]$ and $S[i+1{:}N]$ are assumed to change much slower in time than the local matrices $C[N]$ and $L[i]$. As a result, the local matrices can be propagated independently while keeping $H[i]$ and $S[i+1{:}N]$ fixed (the equations are then decoupled). In Equation (25), the inverse of S would be numerically unstable if some eigenvalues of S are very small. This problem will be severe when the state is weakly correlated (such as a Hartree product state which is usually an initial state) and M_S is much larger than what is required. To some extent, this instability problem makes this evolution scheme paradoxical in that large M_S should in principle push the result to a numerically exact limit but in fact deteriorates it. The same problem also arises in (ML)-MCTDH, where in order to make S more well-conditioned, it is usually replaced with a regularized overlap matrix $\widetilde{S} = S + \varepsilon e^{-S/\varepsilon}$.[21] Here ε is a small scalar commonly from 10^{-8} to 10^{-14}. Most recently, an improved regularization scheme based on the matrix unfolding of the local matrix by SVD in (ML-)MCTDH is proposed by Meyer and Wang, which has been proved to make the time integration more accurate and robust.[121,122] The same idea has also been adopted in TD-DMRG. The readers are referred to Reference 64 for more details.

TDVP-PS

Another EOM is based on the tangent vectors defined with respect to multiple mixed canonical forms as Equation (13). It can be solved using a symmetric second-order Trotter decomposition to split the formal propagator into the individual terms, called projector-splitting algorithm[61,62]:

$$\begin{aligned} e^{-i\widehat{P}\widehat{H}\tau} = &\left[\prod_{i=1}^{N-1} e^{-i\widehat{P}[1:i-1]\bigotimes\widehat{I}_i\bigotimes\widehat{P}[i+1:N]\widehat{H}\tau/2} \cdot e^{i\widehat{P}[1:i]\bigotimes\widehat{P}[i+1:N]\widehat{H}\tau/2}\right] \cdot e^{-i\widehat{P}[1:N-1]\bigotimes\widehat{I}_N\widehat{H}\tau} \\ &\cdot \left[\prod_{i=N-1}^{1} e^{i\widehat{P}[1:i]\bigotimes\widehat{P}[i+1:N]\widehat{H}\tau/2} \cdot e^{-i\widehat{P}[1:i-1]\bigotimes\widehat{I}_i\bigotimes\widehat{P}[i+1:N]\widehat{H}\tau/2}\right] + \mathcal{O}(\tau^3). \end{aligned} \tag{31}$$

Based on the propagator in Equation (31), a single step of time evolution consists of a left-to-right sweep and a subsequent right-to-left sweep each with step size $\tau/2$. Taking left-to-right sweep as an example, the matrix at the canonical center $C[i]$ is firstly evolved forward in time by applying the projector $\widehat{P}[1:i-1]\bigotimes\widehat{I}_i\bigotimes\widehat{P}[i+1:N]$:

$$i\frac{\partial C[i]^{\sigma_i'}_{l_{i-1}'r_i'}}{\partial t}=\sum_{l_{i-1},\sigma_i,r_i} H[i]_{l_{i-1}'\sigma_i'r_i',l_{i-1}\sigma_i r_i} C[i]^{\sigma_i}_{l_{i-1}r_i}, \tag{32}$$

where $H[i]$ and the ingredients $h[1{:}i-1]$, $h[i+1{:}N]$, $h[i]$ all have the same definitions as in Equations (26)–(29) except that the $A[i]$ in Equation (29) is replaced with $L[i]$ or $R[i]$ accordingly. Then, the evolved matrix $C[i]$ is decomposed by QR as Equation (7) to obtain the left-canonical matrix $L[i]$ and $D[i]$. $D[i]$ is evolved backward in time by applying the projector $\widehat{P}[1:i]\bigotimes\widehat{P}[i+1:N]$:

$$i\frac{\partial D[i]_{l_i'r_i'}}{\partial t}=\sum_{l_i,w_i,r_i} h[1:i]_{\{l',w,l\}_i} h[i+1:N]_{\{r',w,r\}_i} D[i]_{l_i r_i}. \tag{33}$$

Afterwards, the canonical center is moved to site $i+1$ by contracting the evolved $D[i]$ and $R[i+1]$ together to obtain $C[i+1]$. Following the procedure above, the sweep continues until all the individual projectors in Equation (31) are applied. Since Equations (32) and (33) are linear, the Krylov subspace method (Lanczos algorithm for Hermitian operator) is preferred as it is unitary and is considered to be better than the explicit time-stepping integrators for matrix exponential operator.[62]

Compared to the P&C schemes, the two schemes TDVP-PS and TDVP-VMF/CMF will not adaptively modify the MPS bond dimension. Additional renormalized states should be constructed smartly to complement the empty renormalized space at the beginning if the initial state is weakly correlated. For instance, propagating the MPS with P&C methods in the first several time steps. For TDVP-PS, inspired by the two-site ground state DMRG algorithm,[36] another way to solve this drawback is to formulate it into a two-site algorithm so that the bond dimension could be changed adaptively.[62,80] However, compared to the standard one-site algorithm, the strict TDVP is violated and in addition, the computational scaling is larger. Recently, further development of the one-site TDVP-PS algorithm is also able to adaptively optimize the bond dimension, which avoids the high-computational cost of the two-site algorithm.[123–125]

Because the TDVP-VMF/CMF scheme and the TDVP-PS scheme are both based on TDVP, $|\Psi(t)\rangle$ should be the same if not considering the error of the integrator. With regard to the time step size, in contrast to P&C-RK, the error will have a monotonic relationship with it. Hence, it is much easier to design an adaptive time-stepping algorithm. For TDVP-VMF, the error estimation with respect to the time step size can be directly incorporated with a minor extra cost because MPS is globally updated (with the standard embedded method RK45,[119] the extra cost is 1/5). For TDVP-PS, which is a local update method, the error due to time step size can only be estimated by calculating the difference between two MPSs $\Psi(t+\tau)$ from the same $\Psi(t)$, one with step size τ and the other with $\tau/2$ (two time steps).[126] In this way, the extra cost is two times. Fortunately, in our experience, TDVP-PS allows a much larger time step size than TDVP-VMF, which overall is more efficient.[64]

2.5 | Finite temperature and mixed state

Because the room temperature is in the same energy scale as the average vibrational frequencies of molecules, it is important to consider the temperature effect when simulating the spectroscopy and dynamics of molecular systems. For example, in steady-state emission spectroscopy, the initial state of the whole system and vibrations consists of a thermal equilibrium ensemble satisfying the Boltzmann distribution. To incorporate the temperature effect, the question is how to first get the thermal equilibrium density matrix and then how to simulate real-time dynamics based on the density matrix.

As the original (TD-)DMRG is a wavefunction theory, the common method to handle temperature is to represent a mixed state density matrix as a wavefunction in the double-space, which is called purification.[50,127] By introducing an auxiliary space Q, any density matrix ρ in the physical space P can be represented as a pure state in the double-space $P\bigotimes Q$. The partial trace of the pure state density matrix over Q recovers the original mixed state density matrix in the P space. The auxiliary space Q can simply be taken as a copy of the physical space P.

$$\rho = \sum_i s_i \,|\, i\rangle\langle i| = \mathrm{Tr}_Q |\Psi\rangle\langle\Psi| \,. \tag{34}$$

$$|\,\Psi\rangle = \sum_i s_i^{1/2} \,|\, i\rangle \,|\, \widetilde{i}\rangle. \tag{35}$$

$|i\rangle$ and s_i are the eigenstate and eigenvalue of ρ. The tilde symbol denotes the Q space state. Equation (35) proves the existence of purified wavefunction. Because $\mathrm{Tr}\rho = 1$, the pure wavefunction is normalized $\langle\Psi|\Psi\rangle = 1$. With this purification method, the number of DoFs is increased from N to 2 N. For a thermal equilibrium density matrix at inverse temperature $\beta = 1/k_B T$, $\rho_\beta = e^{-\beta \widehat{H}_P}/Z(\beta)$ (the partition function $Z(\beta) = \mathrm{Tr}\left(e^{-\beta \widehat{H}_P}\right)$), the corresponding pure thermal state in the double-space is

$$|\,\Psi_\beta\rangle = \sum_{\{\sigma\}} \frac{e^{-\beta \widehat{H}_P/2}}{\sqrt{Z(\beta)}} |\,\sigma_1 \cdots \sigma_N\rangle \,|\, \widetilde{\sigma}_1 \cdots \widetilde{\sigma}_N\rangle. \tag{36}$$

In order to obtain $|\Psi_\beta\rangle$, in the general case, the imaginary-time SE with $\widehat{H} = \widehat{H}_P \bigotimes \widehat{I}_Q$ is integrated from $t = 0$ ($\Psi(0) = \Psi_0$) to $t = -i\beta/2$ ($\Psi(-i\beta/2) = \Psi_\beta$). This method is named imaginary time evolving (ITE) in this review. The initial thermal state corresponds to the mixed state at infinite high temperature $\beta = 0$, in which each physical state is equally populated. Therefore, the initial thermal state is

$$|\,\Psi_0\rangle = \sum_{\{\sigma\}} \frac{1}{\sqrt{d^N}} |\,\sigma_1 \cdots \sigma_N\rangle \,|\, \widetilde{\sigma}_1 \cdots \widetilde{\sigma}_N\rangle = \prod_i \sum_{\sigma_i} \frac{1}{\sqrt{d}} |\,\sigma_i\rangle \,|\, \widetilde{\sigma}_i\rangle. \tag{37}$$

$|\Psi_0\rangle$ is the maximally entangled state between the space P and Q. Fortunately, it can be easily encoded as an MPS through a proper ordering of the DoFs. If the DoFs are ordered as Equation (36), the entanglement between the boundary of P space and Q space (between $|\sigma_N\rangle$ and $|\,\widetilde{\sigma}_1\rangle$) is huge, which will lead to $M_S = d^N$. On the contrary, if the ordering is $|\,\sigma_1\widetilde{\sigma}_1 \cdots \sigma_N\widetilde{\sigma}_N\rangle$, according to Equation (37), only $|\sigma_i\rangle$ and $|\,\widetilde{\sigma}_i\rangle$ are entangled ($M_S = d$), while $|\,\sigma_i\widetilde{\sigma}_i\rangle$ is not entangled with $|\,\sigma_{i\pm1}\widetilde{\sigma}_{i\pm1}\rangle$ ($M_S = 1$). The graphic representation of this proper ordering is shown in Figure 7a. Moreover, $|\,\sigma_i\widetilde{\sigma}_i\rangle$ can be combined into a single super-site with two physical indices (Figure 7b). We prefer this formulation in our works as the local entanglement within each pair of physical-auxiliary DoFs is fully accounted for. However, the side effect is that the computational scaling to handle one site is larger. When integrating the imaginary-time SE, the norm of the wavefunction is not conserved to be 1, as the imaginary-time SE is not unitary. Hence, after each time step, the wavefunction should be normalized again.

The ITE method can be applied to any Hamiltonian to obtain a thermal equilibrium state of the whole Hamiltonian. For system-bath Hamiltonian, this equilibrium state will make the system DoFs and bath DoFs correlated together. In some cases, if only the dynamics of a factorized initial state is of interest, that is, the system and bath are independent at the beginning $\rho(0) = \rho_S \bigotimes \frac{e^{-\beta H_B}}{Z_B(\beta)}$ and only the bath DoFs are in the thermal equilibrium condition, the thermal state can also be factorized $|\Psi_\beta\rangle = |\Psi_S\rangle \bigotimes |\Psi_B\rangle$. In most system-bath model problems, the system part is only composed of a

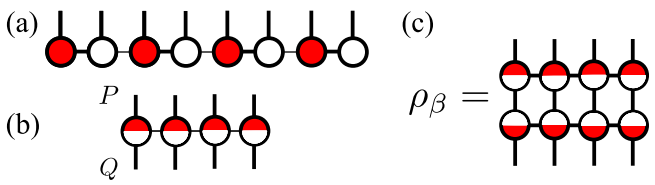

FIGURE 7 The treatment of mixed state density matrix in TD-DMRG by purification method. (a) The pure thermal state in which the physical DoF (red) and the corresponding auxiliary DoF (white) are arranged next to each other. (b) The pure thermal state in which the physical DoF and the corresponding auxiliary DoF are combined into one super-site. (c) The density matrix is obtained after tracing over the auxiliary DoFs

few DoFs, therefore the initial system state $|\Psi_S\rangle$ is assumed to be easily obtained, which fulfills $\rho_S = \mathrm{Tr}_Q(|\Psi_S\rangle\langle\Psi_S|)$. In addition, if the initial system is a pure state $|\phi\rangle$, there is even no need to introduce the auxiliary space Q of the system part, i.e., $|\Psi_S\rangle = |\phi\rangle$. In the system-bath models, the bath part is composed of a bunch of independent harmonic oscillators, $H_B = \sum_k \omega_k b_k^\dagger b_k$. In this case, the bath thermal state has an analytical form if the eigenstate of the harmonic mode $|n_k\rangle$ is used as the primitive basis,

$$|\Psi_B\rangle = \prod_k \sum_n \frac{e^{-\beta n_k \omega_k/2}}{\sqrt{Z_B(\beta)}} |n_k\rangle |\tilde{n}_k\rangle. \tag{38}$$

Apparently, each physical mode is only entangled with its corresponding auxiliary mode. This entanglement, however, can be fully removed through the so-called thermal Bogoliubov transformation over each pair of physical-auxiliary modes,[128–131]

$$\begin{aligned} |\Psi_B\rangle &= e^{iG} \prod_k |0_k \tilde{0}_k\rangle \\ G &= -i \sum_k \theta_k \left(b_k^\dagger \tilde{b}_k^\dagger - b_k \tilde{b}_k \right), \ \theta_k = \mathrm{arctanh}\left(e^{-\beta\omega_k/2}\right). \end{aligned} \tag{39}$$

This method is called the thermo field dynamics (TFD). To get Equation (39), the equation $e^{\theta\left(b^\dagger \tilde{b}^\dagger - b\tilde{b}\right)} = e^{\tanh(\theta) b^\dagger \tilde{b}^\dagger} e^{-\ln\cosh(\theta)\left(b^\dagger b + \tilde{b}^\dagger \tilde{b} + 1\right)} e^{-\tanh(\theta) b\tilde{b}}$ is used.[132] After this similarity transformation, new quasi-modes are introduced which mix the P space mode and Q space mode together.

$$e^{-iG} b_k e^{iG} = b_k \cosh(\theta_k) + \tilde{b}_k^\dagger \sinh(\theta_k). \tag{40}$$

$$e^{-iG} \tilde{b}_k e^{iG} = \tilde{b}_k \cosh(\theta_k) + b_k^\dagger \sinh(\theta_k). \tag{41}$$

The new effective Hamiltonian is $\widehat{\overline{H}} = e^{-iG} \widehat{H} e^{iG}$. We will give the explicit form of the effective Hamiltonian of Holstein model in Section 3.2. The new thermal state is $|\overline{\Psi}_\beta\rangle = |\Psi_S\rangle \prod_k |0_k \tilde{0}_k\rangle$. The bath thermal state $\prod_k |0_k, \tilde{0}_k\rangle$ is a non-entangled Hartree product state, which is also called thermal vacuum in TFD. It can be efficiently represented by an MPS with $M_S = 1$. After this transformation, the finite temperature dynamics is reduced to zero temperature dynamics with "renormalized" Hamiltonian. The bath excitations can only be created dynamically through the interaction with the system. We note that a similar idea to treat the temperature effect in the condensed phase has been proposed by representing the finite temperature bath correlation function (BCF) of the original BSD as a zero temperature BCF of an effective BSD, which is extended to the negative frequency domain.[133] It is also worth mentioning that a similar thermal Bogoliubov transformation can be applied to a free fermionic system to obtain a thermal equilibrium state.[128]

Actually, the purification methods are closely related to the conventional double-space formulation of density matrix theory, that is, the $N \times N$ density matrix in the Hilbert space is reshaped to a N^2-length vector in the Liouville space. In this sense, the thermal state is the square root of the original density matrix, $|\Psi_\beta\rangle = \rho_\beta^{1/2}$. That is why TFD is also called the symmetric representation of double-space formulation.[134] This isomorphic relation between $|\Psi_\beta\rangle$ and $\rho_\beta^{1/2}$ is also indicated in the super-site representation in Figure 7b, which is in fact of an MPO structure.[135] Based on the conventional double-space formulation, the imaginary-time SE can be integrated from 0 to $-i\beta$ to directly obtain ρ_β. However, in practice, the resulting ρ_β is not as accurate and efficient as the purification method if the bond dimension is the same. It is not only because ρ_β in the purification method has $M_D = M_S^2$, but also because the evolving time is only half, which indicates a smaller numerical error and cost. Coincidentally, in the original two papers extending TD-DMRG to finite temperature case, one is formulated following purification method,[136] another is formulated following

the conventional Liouville double-space formulation.[137] The second difference between the purification method and the conventional double-space formulation of density matrix theory is that for independent bosons or fermions, TFD can adopt thermal Bogoliubov transformation to introduce new quasi-particles, which will disentangle the entanglement between the double-space of the thermal state.

If the real-time dynamics of the mixed state is governed by the von Neumann equation $i\partial\rho(t)/\partial t = \left[\widehat{H}_P(t), \rho(t)\right]$, it is equivalent to evolving the thermal state $|\Psi(t)\rangle$ according to SE and then the expectation value of any operator can be calculated as $\mathrm{Tr}\left(\widehat{O}\rho(t)\right) = \langle\Psi(t)|\widehat{O}|\Psi(t)\rangle$. One good feature of the purification method for real-time dynamics is that in principle the following three conditions can be fulfilled if proper wavefunction evolution schemes such as TDVP-based algorithms are used: (i) $\mathrm{Tr}\rho(t) = 1$; (ii) $\rho(t) = \rho(t)^\dagger$; (iii) $\rho(t)$ is positive semi-definite. In addition, in the purification method, any unitary transformation can be applied to the DoFs in the Q space, which will not change the physical $\rho(t)$ ($\mathrm{Tr}_Q\left(\widehat{U}_Q\,|\,\Psi\rangle\langle\Psi\,|\,\widehat{U}_Q^\dagger\right) = \mathrm{Tr}_Q(|\,\Psi\rangle\langle\Psi\,|)$). Inspired by this property, several works proposed to use $\widehat{H} = \widehat{H}_P - \widehat{H}_Q$ to propagate the Q space backward, which hopefully can alleviate the growth of entanglement caused by the forward propagation in the P space.[138] However, when ρ follows dissipative dynamics, for example, it is governed by the Lindblad master equation,

$$\partial\rho(t)/\partial t = -i\left[\widehat{H}, \rho(t)\right] + \sum_i \left(L_i\rho(t)L_i^\dagger - \frac{1}{2}\left\{L_i^\dagger L_i, \rho(t)\right\}\right), \tag{42}$$

it is extremely difficult to find a time evolution equation of the pure thermal state. In this case, one should resort to the conventional Liouville double-space formulation instead of purification in order to simulate dissipative systems.[86,137,139–141] In this case, the former three physical conditions cannot be fully fulfilled. Recently, Shi et al. incorporated another constraint $\mathrm{Tr}(\partial\rho(t)/\partial t) = 0$ in the original TDVP equation through the Lagrange multiplier method, which can successfully alleviate this problem.[139]

Except for the cases that the analytical thermal Bogoliubov transformation can apply, the purification method is not efficient to obtain the thermal equilibrium state at a very low temperature (β is very large), because of the accumulated error in the numerical imaginary time evolution. To handle low temperature, Stoudenmire and White proposed a method called the minimally entangled typical thermal states (METTS), which samples the thermal ensemble to obtain the thermal properties. We refer the interested readers to Reference 46 for more details. How effective METTS is in the electron–vibration coupled problems is still an open question.

2.6 | Multiset ansatz

For vibronic problems, considering the wavepacket on different PESs would be quite different, it is more appropriate to use several MPSs together to describe the whole wavefunction, each corresponding to one PES. This extension of TD-DMRG is called the multiset method,[74] which is originally proposed in MCTDH to solve nonadiabatic dynamics between several PESs.[142] The wavefunction ansatz is

$$|\,\Psi\rangle = \sum_i c_i\,|\,i\rangle\,|\,\Psi_{\mathrm{MPS}}\rangle_i, \tag{43}$$

$|i\rangle$ is the electronic state and $|\Psi_{\mathrm{MPS}}\rangle_i$ is the wavepacket on each PES. The multiset method would be more effective than the common single-set method in that the primitive basis and $|\Psi_{\mathrm{MPS}}\rangle_i$ can be optimized for a specific PES and the overall wavefunction could be more compact.

2.7 | Ordering problem and other TNS

As introduced above, for systems of general interaction topology, MPS is not as efficient as for 1-D nearest-neighbor interaction topology. In practice, to reduce the entanglement at each boundary as much as possible, the ordering of DoFs in MPS is an important aspect to consider when mapping the DoFs of arbitrary interaction topology to a 1-D

chain. It is widely accepted that DMRG will be more accurate if the most entangled DoFs are arranged closely. With a given bond dimension, a larger distance between two entangled DoFs in the MPS chain indicates a larger renormalization error. A typical example is the thermal state at infinite high temperature in Section 2.5, in which different ordering of the physical and auxiliary DoFs will result in a huge difference in the bond dimension of the MPS. With this philosophy, several algorithms have been proposed to optimize the ordering, most of which are for molecular electronic structure problems.[143–147] Among them, several algorithms are possible to be extended to the time-dependent problems, such as the quantum entropy based ordering algorithm.[143,145] Different from the ground state problem, the time-dependent problem is more complicated in that the entanglement will vary with time. How to utilize the time-dependent quantum entropy to optimize the ordering is still an open question.

Optimizing the order will only partly alleviate the problem of 1-D parameterization for general systems of long-range interactions, because the average distance between two DoFs in MPS is always $\mathcal{O}(N)$. More complicated TNS beyond 1-D structure have been developed in order to capture more entanglement, some of which have been used in the calculation of molecular electronic eigenstate, vibrational eigenstate, and in the simulation of quantum dynamics.[65,66,68,79,99,148–150] Tree TNS is a direct generalization of MPS in which each site is linked to more than two other sites.[65,68] With this structure, the average distance between two DoFs is $\mathcal{O}(\log N)$. With the same bond dimension as MPS, it in principle should be more accurate to approximate a general state. The structure of TTNS is very flexible. One common structure is that each node has one physical index and more than two virtual indices (Figure 8a), therefore the number of nodes is still N but the computational scaling to handle each node is much larger than MPS, especially in the two-site algorithm.[65] To overcome this, the three-legged TNS (T3NS) has been proposed, in which the nodes with physical indices are separated by the nodes with only three virtual indices (Figure 8b, the nodes with physical indices are indicated in red, the others are indicated in blue).[66] With this structure, each node has only three indices and thus the computational scaling is lower than the standard TTNS. Interestingly, from the TNS point of view, ML-MCTDH has a TTNS wavefunction ansatz with all physical indices attached in the leaf node (the bottom layer),[68] which is mathematically called hierarchical Tucker format (Figure 8c shows an ML-MCTDH wavefunction with a binary tree structure). The standard MCTDH also belongs to one kind of TNS, in which the core tensor is still exponentially large but with a smaller base (Figure 8d). From this starting point, it is proposed to use the MPS structure to decompose the core tensor (Figure 8e).[148] The exact same structure has been proposed in a former study, taking MPS as the starting point, called the optimized boson basis

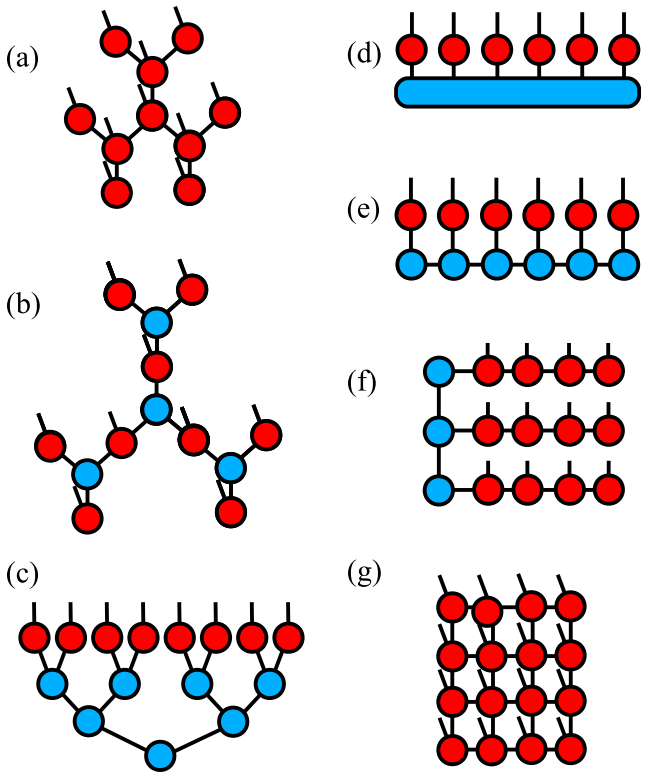

FIGURE 8 The graphic representation of representative tensor network states. (a) TTNS, (b) T3NS, (c) ML-MCTDH, (d) MCTDH, (e) OBB, (f) comb TNS, and (g) PEPS

(OBB) method, in order to solve the problem that the size of the primitive basis for each mode needs to be extremely large in some parameter regime.[149,151] In some systems, the interaction topology can be divided into several subunits/fragments, for example, in the molecular aggregates each molecule has a local bath, these bath DoFs are not directly interacted. In this case, the bath DoFs of each molecule can be gathered in one chain, and the electronic DoFs are arranged in the main trunk or simply combined into one super-site (Figure 8f). This TNS structure is named comb TNS or multi-chain TNS.[79,150] The above TNSs share one common feature that there is no loop in the TNS—cutting one virtual bond will divide the TNS into two parts. However, it has been known that for some problems only TNS with loops can effectively capture the entanglement, for example, for a 2-D lattice model, only PEPS can fulfill the area law (Figure 8g).[67] The drawbacks are that (i) The computational scaling of contracting TNS with loops is much higher than the competitors without loops. For example, when contracting two PEPSs to calculate the overlap, the exact algorithm will give an exponential scaling. Only approximate algorithms are practically affordable, which are still very expensive.[67] (ii) Because of the closed loops, when updating one single site during the sweep procedure, it is not possible to define the canonical form as TNS without loops. This will bring numerical stability issues. For example, when optimizing a single site in a variational way to target the ground state, a generalized eigenvalue equation, $H^{\text{eff}}c = \lambda Sc$, should be solved. In TNS without loops, the canonical form will ensure the overlap matrix S to be identity, but in TNS with loops, S may be not well conditioned, which would lead to numerical instability.[67] Both of these two drawbacks prevent TNS with loops from being used in complex systems. In summary, TNSs developed from MPS are in principle more accurate for problems with general interaction topologies, but the challenge is that their computational scaling is also higher than that of MPS. How to design tensor networks that conform most to the interaction topology is one of the most critical issues to address before it could become a practical approach for quantum dynamics.

2.8 | CPU-GPU heterogeneous programming

The progress of efficient numerical methods cannot be achieved without the support of hardware. The algorithms of TD-DMRG are composed of lots of tensor contractions and tensor decompositions. It is much more efficient to use GPU than the common CPU to calculate the tensor contractions, while the tensor decomposition is hard to parallelize with GPU. We proposed to use CPU-GPU heterogeneous programming to accelerate TD-DMRG calculations, in which GPU is responsible for tensor contraction and CPU is responsible for tensor decomposition. This simple strategy to assign the jobs to different hardware will speed up TD-DMRG from several to tens of times.[64] The results will be shown in Section 3.2.

3 | BENCHMARKS

There are several benchmarking systems for the quantum dynamics methods, such as the SBM, the Frenkel–Holstein model. In both models, we will first show the accuracy of TD-DMRG compared with the established numerically exact methods. In addition, in SBM, we focus on the computational scaling of TD-DMRG. In the Frenkel–Holstein model, we focus on the two slightly different algorithms of TD-DMRG to handle finite temperature introduced in Section 2.5—ITE and TFD.

3.1 | Spin-boson model

SBM is one of the simplest but nontrivial models to study open quantum dynamics, describing the behavior of a spin interacting with a bosonic environment.[7] The Hamiltonian is written as

$$\widehat{H} = \epsilon\sigma_z + \Delta\sigma_x + \sum_k \frac{1}{2}\left(\widehat{p}_k^2 + \omega_k^2\widehat{x}_k^2\right) + \sigma_z\sum_k c_k\widehat{x}_k. \tag{44}$$

$\widehat{x}_k$ and $\widehat{p}_k$ are the coordinate and momentum of bath DoF respectively. ω_k is the vibrational frequency. c_k is the coupling constant. For systems in the condensed phase, the system-bath coupling is characterized by a bath spectral density function

$$\mathcal{J}(\omega)=\frac{\pi}{2}\sum_k \frac{c_k^2}{\omega_k}\delta(\omega-\omega_k). \tag{45}$$

With Ohmic ($s=1$) and sub-Ohmic ($s<1$) spectral density $\mathcal{J}(\omega)=\frac{\pi}{2}\alpha\omega^s\omega_c^{1-s}e^{-\omega/\omega_c}$, it is known that unbiased SBM at zero temperature will undergo a delocalization to localization quantum phase transition with the increase of the system-bath coupling strength α (Kondo parameter). Below the critical value α_c, the spin state will be delocalized with $\langle\sigma_z\rangle=0$ in the steady state; in addition, the spin dynamics gradually changes from coherent decay to incoherent decay as α increases. Further increasing α above α_c will push SBM into the localized phase with $\langle\sigma_z\rangle\neq 0$ in the steady state.[7,88] Because of the simplicity of the model and the nontrivial behavior, SBM has been widely used to benchmark different methods. It is worth mentioning that Wang et al. have carried out extensive numerically exact calculations on SBM at zero temperature with ML-MCTDH covering a quite broad parameter regime.[22,23]

We benchmark TD-DMRG in the unbiased SBM ($\epsilon=0$, $\Delta=1$) with the sub-Ohmic spectral density ($s=0.5$) from weak $\alpha=0.05$ to strong $\alpha=1.0$ coupling strength. The frequency cutoff is $\omega_c=20$. For the open quantum systems, TD-DMRG treats the whole system and bath after a proper discretization together as a closed system. Here, the BSD is discretized through the same scheme used in Reference 23.

$$\int_0^{\omega_j} d\omega\rho(\omega)=j,\quad j=1,\ldots,N_b. \tag{46}$$

$$\rho(\omega)=\frac{N_b+1}{\omega_c}e^{-\omega/\omega_c}. \tag{47}$$

$\rho(\omega)$ is the chosen density of states, which is large in the important low-frequency region. N_b is the number of discrete modes. The contribution of the higher frequency part beyond the highest discrete frequency ω_{N_b} is considered through the adiabatic renormalization method, which slightly modifies the electronic coupling Δ.[7] The initial state is a spin-up state with all vibrations in the ground state. In the setup of TD-DMRG calculations, the bond dimension is $M_S=20$, the size of SHO basis for each bath DoF is $d=10$ and the TDVP-PS evolution scheme is used. The sites are ordered with the spin in the first position, followed by the vibrational DoFs from low to high frequency. All the TD-DMRG calculations in this and the next section are carried out with the open-source package RENORMALIZER developed by us.[152] The results with $N_b=1000$ and different coupling strengths α are shown in Figure 9a. The dashed colored lines are the results of TD-DMRG, which are consistent well with the available ML-MCTDH results. To show the efficiency of TD-DMRG, the wall-time of TD-DMRG calculations ($\alpha=0.05$, $\tau=0.1$, $t=200$, $M_S=20$, $d=10$) with respect to different number of modes N_b (up to 5000) using one CPU core is shown in Figure 9b. As discussed above, with fixed M_S, the wall-time is almost linear with N_b as expected. From this figure, the readers can get a feeling for the size of the system

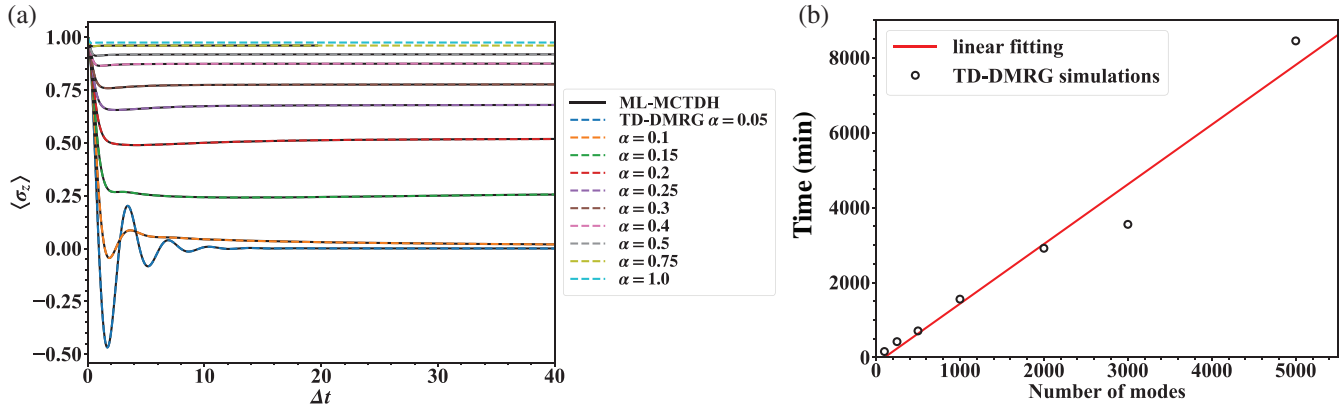

FIGURE 9 (a) The population dynamics of SBM ($\epsilon=0$, $\Delta=1$) with sub-Ohmic spectral density ($s=0.5$, $\omega_c=20$) from weak coupling $\alpha=0.05$ to strong coupling $\alpha=1.0$. The colored dashed lines are the results of TD-DMRG with $M_S=20$, $d=10$. The black solid lines are the results of ML-MCTDH from Reference 23 with α from 0.05 to 0.75. (b) The wall-time of TD-DMRG calculations using one Intel Xeon Gold 5218R CPU @ 2.10GHz core ($\alpha=0.05$, $\tau=0.1$, $t=200$, $M_S=20$, $d=10$) with different number of discrete modes N_b. The red line is the linear fitting of the actual data points. The TDVP-PS evolution scheme is used

that the standard TD-DMRG can handle nowadays. Higher efficiency will be gained if the same technique as the ML-MCTDH simulations in References 22, 23, 140 are adopted, which combines several DoFs into one super-site and limits the total number of excitation quanta within each super-site.

To better show the actual computational scaling of TD-DMRG, we further simulate SBM ($s = 0.5$, $\alpha = 0.05$) with different sizes of bond dimension M_S and different sizes of primitive basis d. For comparison, we also use ML-MCTDH to do the same calculations. The comparison of the efficiency of these two methods previously focused on the eigenvalue problems.[153] Here, we focus on the time evolution problems. The Heidelberg MCTDH package (version 8.5) is used for ML-MCTDH calculations.[154] Although it may be not appropriate to directly compare the computational time of two different packages because the performance depends on many aspects, we hope it can still fairly show the computational scaling of these two methods at least with the standard implementation. Despite that the tree structure of ML-MCTDH can be quite flexible, we use the binary tree and the ternary tree structures for simplicity. The spin node is attached to the top layer. In ML-MCTDH, the single-particle functions (SPFs) play the same role as the renormalized states in DMRG. Thus, for convenience, we also call the size of SPFs bond dimension M_S. They are set to be the same as TD-DMRG. Additionally, in the bottom layer, when $M_S > d$, two (binary tree) or three (ternary tree) primitive modes are directly linked to the next layer; when $M_S < d$, each primitive mode is first contracted to M_S SPFs and then linked to the next layer. In TD-DMRG, the TDVP-VMF evolution scheme is used for a fair comparison, though it is not as efficient as TDVP-PS. The other parameters are described in detail in the caption of Figure 10. In the calculations, the most time-consuming procedure is the contraction of the whole tensor network in calculating $\left\langle \partial\Psi/\partial A_i|\widehat{H}|\Psi\right\rangle$ (A_i is the matrix of each node). Figure 10a shows that the computational cost of TD-DMRG is linearly proportional to N_b (same as Figure 9b), while that of ML-MCTDH is quadratic. This is due to that ML-MCTDH calculates each term of Hamiltonian separately. In SBM, the number of terms in Hamiltonian is $\mathcal{O}(N_b)$. For each term, there are $\mathcal{O}(N_b)$ local tensors that should be contracted. Hence, the overall cost of ML-MCTDH is $\mathcal{O}(N_b^2)$. In TD-DMRG, the Hamiltonian is treated as a single MPO. Because M_O of SBM is only 3 independent of N_b, the cost is $\mathcal{O}(N_b)$. This advantage of TD-DMRG over ML-MCTDH due to MPO has also been found in the calculation of the ground state of linear rotor chains.[153] Therefore, it is important to introduce MPO (or the generalized tensor network operator) for efficient tensor network simulation. Figure 10b shows the computational cost with different bond dimensions M_S. The scaling of TD-DMRG is $\mathcal{O}(M_S^3)$ as a result of the contraction of two nodes each with two virtual indices. For the same reason, in ML-MCTDH, the scaling of contracting two nodes except the bottom layer is $\mathcal{O}(M_S^4)$ for the binary tree and $\mathcal{O}(M_S^5)$ for the ternary tree as the number of virtual indices is 3 and 4 respectively. Hence, MPS is more efficient than ML-MCTDH if a large bond dimension is used. However, it should be noted that since the tree structure is in principle can capture more entanglement than MPS, a smaller bond dimension can be used. Whether the reduction in the bond dimension can compensate for the larger scaling depends on the specific problem.[65] Figure 10c shows the computational cost with the size of primitive basis d. Surprisingly, the cost of ML-MCTDH is almost independent of d when $d > M_S$. This is due to the switch of the tree structure after $d > M_S$ discussed above. It leads to that the cost of contracting the bottom layer containing the physical indices is negligible (formally $\mathcal{O}(d)$ using the DVR basis) compared to the contraction of the upper layer. In TD-DMRG, the computational scaling to contract the physical indices is $\mathcal{O}(d^2)$. Hence, for problems in which a large primitive basis set is necessary, such as the critical and strong coupling phases of SBM with large bosonic shifts,[149] ML-MCTDH is more efficient than TD-DMRG. Learning from ML-MCTDH, the $\mathcal{O}(d)$ scaling can be achieved

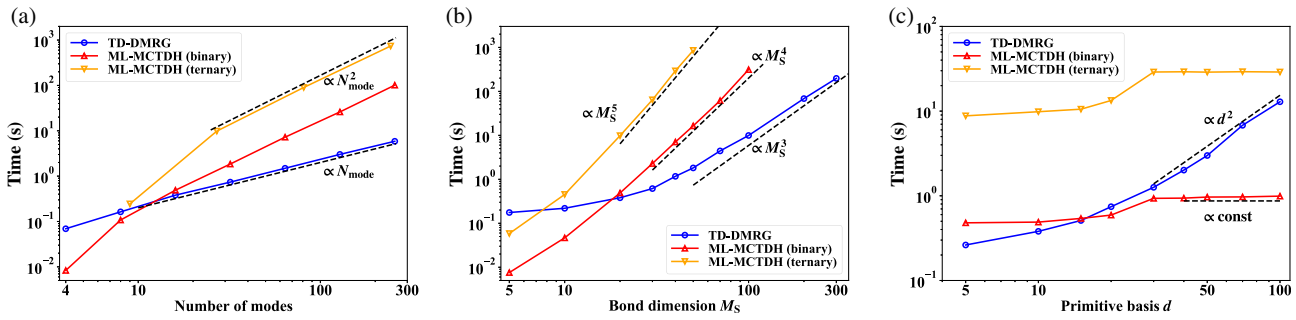

FIGURE 10 The computational cost of single evolution step in TD-DMRG and ML-MCTDH (binary tree and ternary tree structure, the spin node is attached to the top layer) on one Intel Xeon CPU E5-2680 v4 @ 2.40GHz core. The TDVP-VMF evolution scheme is used in both methods with relative error threshold 10^{-5} and regularization parameter $\varepsilon = 10^{-8}$. (a) $M_S = 20$, $d = 10$, N_b varies. (b) $N_b = 16$, $d = 10$, M_S varies. (c) $N_b = 16$, $M_S = 20$, d varies. The black dashed line is a guide to indicate the polynomial scaling

in MPS by using the DVR basis to diagonalize the potential operator and treating the MPO as sparse matrices. Besides ML-MCTDH, the OBB tensor network structure in Figure 8e, which resembles MPS the most, can also solve this problem. However, the scaling of the OBB structure with respect to M_S is increased to $\mathcal{O}(M_S^4)$.

3.2 | EET in Fenna–Matthews–Olson complex

The second test-bed is the dynamics of EET in the Fenna–Matthews–Olson complex, which is a pigment–protein complex mediating the EET process from light-harvesting chlorosomes to the reaction center during the photosynthesis in green sulfur bacteria.[155] In the two-dimensional electronic spectroscopy study, a long-lasting beating signal over several hundred femtoseconds at room temperature was found, which indicates the quantum coherence and wave-like EET in the noisy biological environment beyond the common expectation.[1,155] The EET process in FMO is described by the Frenkel–Holstein model,[1,71,86] which is written as Equation (48) in the second quantization.

$$H=\sum_i \varepsilon_i a_i^\dagger a_i+\sum_{ij} V_{ij} a_i^\dagger a_j+\sum_{ik}\omega_{ik} b_{ik}^\dagger b_{ik}+\sum_{ik} g_{ik}\omega_{ik} a_i^\dagger a_i\left(b_{ik}^\dagger+b_{ik}\right). \tag{48}$$

In this model, ε_i is the local excitation energy of the ith pigment. V_{ij} is the excitonic coupling between them. Each pigment has an independent bath with vibrational frequency ω_{ik} and coupling constant g_{ik}. The real-time dynamics of the EET process in FMO has been simulated by many numerical methods and thus it serves as a good reference to benchmark TD-DMRG.[73,86,140,156] We simulate the dynamics of the 7-site FMO model at 77 K with a factorized initial state $\rho(0)=|1\rangle\langle 1|\bigotimes\rho_B^{\mathrm{eq}}$. The parameters adopted are the same as References 140, 156, 157. The experimental spectral density for one pigment is discretized into 74 modes at equal intervals. The number of SHO bases for each mode is $d=10$. The TDVP-PS evolution scheme is used. The result of HEOM combined with the hierarchical Tucker ansatz (HEOM-HT), which is recently developed by Shi and coworkers,[140] is adopted as a reference. We will compare the performance of two finite temperature TD-DMRG algorithms, ITE and TFD. The site ordering is that the vibrational DoFs are first ordered by molecular index, and the vibrations of the same molecule are arranged together from lowest to highest frequency. The electronic DoF is placed in the middle of the whole chain. In ITE, the corresponding physical and auxiliary DoFs are combined into one super-site. While in TFD, they are placed next to each other as discussed in Section 2.5.

Since any unitary transformation in the auxiliary Q space will not affect the P space dynamics, in TFD, the augmented Hamiltonian in the $P\bigotimes Q$ space is commonly constructed as $H-\sum_{ik}\omega_{ik}\tilde{b}_{ik}^\dagger\tilde{b}_{ik}$. After thermal Bogoliubov transformation ($G=\sum_i G_i$, G_i is the same as Equation (39)), the effective Hamiltonian is

$$\begin{aligned}\overline{H}&=e^{-iG}\left(H-\sum_{ik}\omega_{ik}\tilde{b}_{ik}^\dagger\tilde{b}_{ik}\right)e^{iG}\\&=\sum_i\varepsilon_i a_i^\dagger a_i+\sum_{ij}V_{ij}a_i^\dagger a_j+\sum_{ik}\omega_{ik}\left(b_{ik}^\dagger b_{ik}-\tilde{b}_{ik}^\dagger\tilde{b}_{ik}\right)\\&\quad+\sum_{ik}g_{ik}\omega_{ik}a_i^\dagger a_i\left[\cosh(\theta_{ik})\left(b_{ik}^\dagger+b_{ik}\right)+\sinh(\theta_{ik})\left(\tilde{b}_{ik}^\dagger+\tilde{b}_{ik}\right)\right]\end{aligned}. \tag{49}$$

In the effective Hamiltonian, the electron–phonon coupling strengths are renormalized by the temperature. At zero temperature, $\theta_{ik}=0$, $\sinh(\theta_{ik})=0$, $\cosh(\theta_{ik})=1$, the P and Q space are disentangled. In this case, the effective Hamiltonian (except the auxiliary bath energy) returns exactly back to the original Hamiltonian.

We compare the populations of TD-DMRG calculated by TFD with that of HEOM-HT in Figure 11a with different M_S. Although not fully converged, $M_S=16$ has already been able to obtain quite good results. The discrepancy can only be seen in the pigments whose population is smaller than 0.1. The results of $M_S=256$ agree well with that of HEOM-HT within 1 ps. Furthermore, comparing the results of TFD and ITE, Figure 11b shows that both of them obtain similar results either at $M=32$ (upper panel) or $M=128$ (lower panel), even though TFD has disentangled the P and Q space at $t=0$ and renormalized the system-bath coupling. The reason is that the thermal Bogoliubov transformation in TFD actually only transforms within each pair of physical-auxiliary modes. Therefore, the inter-pair entanglement between

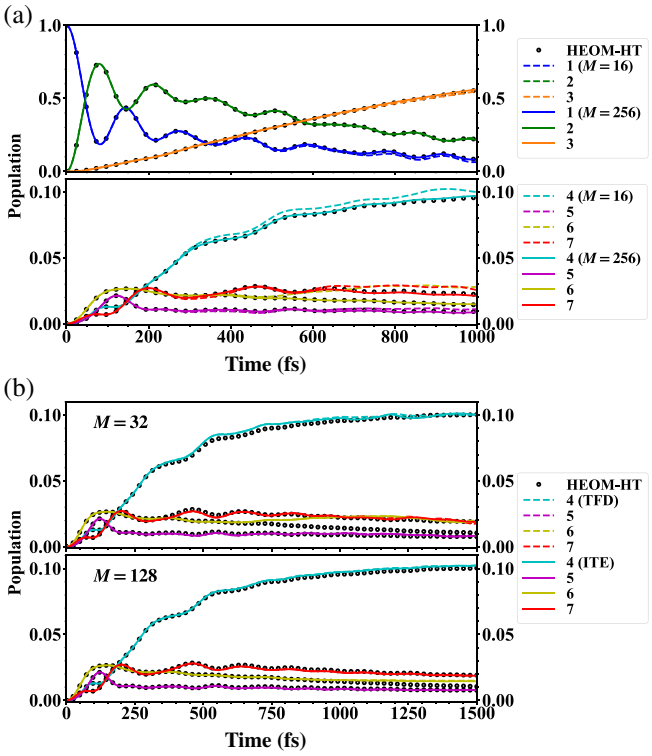

FIGURE 11 The population dynamics of the 7-site FMO complex at 77 K. (a) The colored lines are results of TD-DMRG by TFD with $M = 16$ (dashed) and $M = 256$ (solid). (b) The colored lines are results of TD-DMRG by TFD (dashed) and by ITE (solid). The black circles are results of HEOM-HT from Reference 140

the different pairs of physical-auxiliary modes established in the real-time dynamics is in principle the same in these two methods. Since the super-site formulation we use in ITE (shown in Figure 7b) treats the intra-pair entanglement exactly, the probable advantage of TFD in reducing the intra-pair entanglement is not demonstrated. Although the accuracy is similar, the computational cost of TFD is much smaller than that of ITE, because the cost of TFD is roughly twice that of zero temperature calculation ($N \to 2N$) with the same M_S but the cost of ITE is roughly $d \sim d^2$ times larger because of one extra physical index in each site. Therefore, for a system-bath problem with a factorized thermal initial state and a free bosonic bath, TFD is more recommended than the ITE method. However, for problems that the initial system-bath correlation is essential, such as emission spectroscopy of molecular aggregates, ITE is the only choice.

Besides the population dynamics, the dipole–dipole time correlation function (Equation (50)) of the 7-site FMO model is also calculated at 77 K, which gives the linear absorption spectrum after Fourier transformation.

$$C_{\mu\mu}(t) = \frac{1}{3}\sum_{\alpha=x,y,z}\langle\hat{\mu}_\alpha(t)\hat{\mu}_\alpha\rangle_T. \tag{50}$$

$\hat{\mu} = \sum_{i=1}^{7}\vec{\mu}_i\left(a_i^\dagger + a_i\right)$ is the transition dipole operator. The transition dipole moment $\vec{\mu}_i$ of each pigment is assumed to be oriented along the connection line of two nitrogen atoms N_B–N_D. The structure is obtained from the protein data bank.[158] $\langle\cdot\rangle_T$ stands for the thermal average. The results calculated by TD-DMRG/TFD and HEOM-HT[140] are shown in Figure 12. A fairly good result can already be obtained with $M_S = 8$, where the difference shows up after 700 fs. With $M_S = 32$, the result of TD-DMRG is consistent with that of HEOM-HT up to 2 ps.

Figure 13 shows the time cost of several time evolution schemes in simulating the EET process in FMO at 0 K with $M_S = 128$.[64] By analyzing the computational cost of each procedure in TD-DMRG, we can find that in the TDVP-based evolution algorithms, the tensor contraction will consume more than 80% of the total time. While in the P&C-RK4 algorithm, besides the tensor contraction, the tensor decomposition of MPS with large bond dimension such as $\hat{H}\,|\,\Psi\rangle$ will also occupy 40%. Simply using the multiple CPU core parallelization implemented in the standard linear algebra

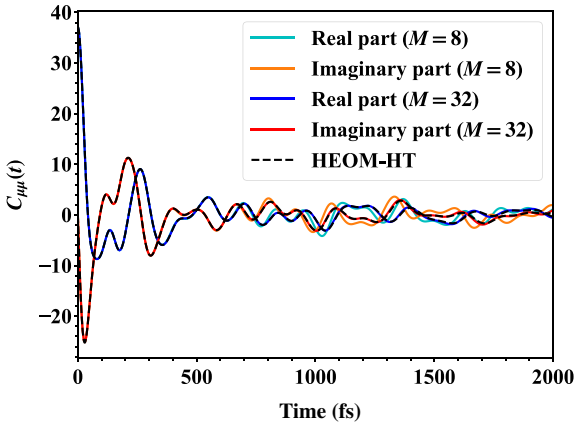

FIGURE 12 The dipole–dipole time correlation function calculated by TD-DMRG/TFD with $M = 8$ and $M = 32$. The black dashed lines are results of HEOM-HT.[140]

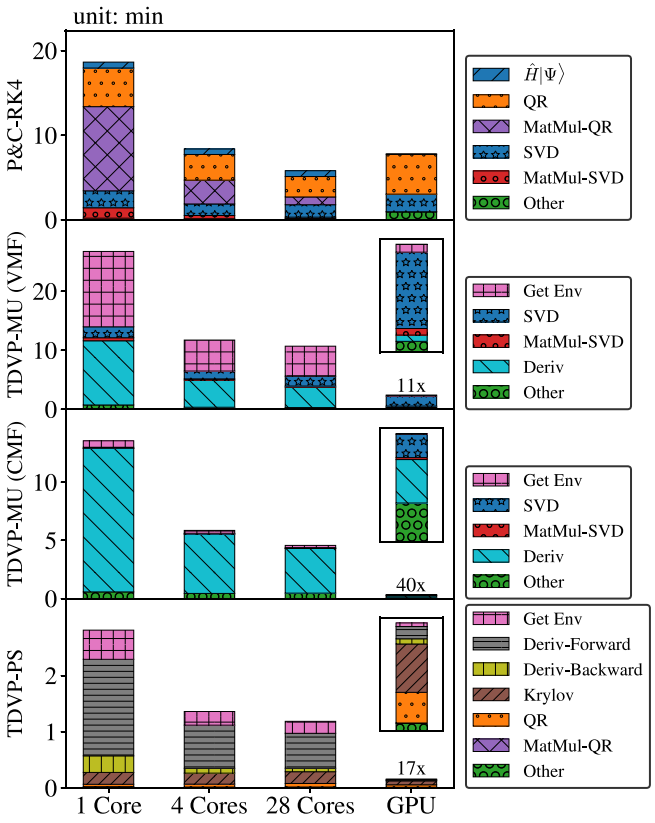

FIGURE 13 The time cost of a single evolution step and its intensive sub-steps with $M_S = 128$ and $\tau = 160$ a.u. by different time evolution schemes in Section 2.4. The bars for CPU-GPU heterogeneous computation are further shown in the insets for clarity (see the text in Reference 64 for the definitions and labels of the sub-steps. Reprinted with permission from Reference 64)

libraries such as the Intel Math Kernel Library can merely accelerate the calculations by a factor of 3. As we discussed in Section 2.8, GPU is well suited for tensor contraction. With one NVIDIA Tesla V100 GPU, the TDVP-based evolution algorithms are accelerated by a factor of 10 to several dozens. The remaining part is mainly composed of the tensor decompositions. With larger M_S, the acceleration will be more prominent. However, the P&C-RK4 evolution scheme is not improved because of the large portion of tensor decomposition.

4 | APPLICATIONS

The developments of TD-DMRG methodology in recent years have enabled its application to a variety of significant scientific problems.[58,59,63,64,70–85] Among them, the majority are focused on open quantum systems, especially with harmonic bath and linear system-bath coupling, to study the quantum dissipation in the condensed phase. Only a few of them are focused on molecular systems. In this section, we choose two examples of applications corresponding to the condensed phase dynamics and gas phase dynamics respectively. The first one is the calculation of the charge mobility of molecular crystals.[77,78] The second one is the calculation of the molecular radiationless decay rates with an anharmonic PES.[81,82]

4.1 | Charge mobility and spectral function of rubrene crystal

The theoretical and computational study of charge transport in the organic molecular crystal has a rather long history but what the intrinsic charge transport mechanism is and how to accurately calculate the charge mobility still have not been fully resolved.[3–5] Several popular theories and their corresponding computational methods have been proposed[159,160]: (i) The charge is fully localized on a single molecule and the transport consists of successive hoppings between neighboring molecules. The semi-classical Marcus theory or full-quantum Fermi's golden rule (FGR) is adopted to calculate the hopping rate. (ii) The charge transport is limited by the low-frequency intermolecular vibrations (dynamic disorder), which induce transient charge localization. (iii) The charge is wavelike as in the common inorganic materials, which has a well-defined quasi-momentum and is scattered by the phonons. The mobility can be calculated by the band theory combined with the Boltzmann transport theory. The complexity of this problem lies in that the physical quantities—electronic transfer integral, vibrational frequency, reorganization energy, room temperature, are almost on the same energy scale, which cannot be separated safely. As a result, it is hard to assign the charge transport in molecular crystal to a specific regime—localization or delocalization, adiabatic or nonadiabatic regimes. Actually, many systems are in the so-called intermediate coupling regime. That is why the former three popular theories have their own "Achilles' heel" and will fail sometimes. The numerically exact TD-DMRG method can in principle treat all the DoFs and interactions on an equal footing, and thus it has the hope to give an unbiased picture. We studied the charge transport in rubrene crystal, which is anisotropic, forming a quasi-one-dimensional transport channel.[77,78] The model used to describe the charge transport of rubrene crystal is the 1-D Holstein–Peierls model, which includes both intramolecular and intermolecular vibrations.

$$\begin{aligned} H = &\sum_i -V\left(a_{i+1}^\dagger a_i + a_i^\dagger a_{i+1}\right) + \sum_{ik} \omega_k b_{ik}^\dagger b_{ik} + \sum_i \nu d_i^\dagger d_i \\ &+ \sum_{ik} g_k \omega_k \left(b_{ik}^\dagger + b_{ik}\right) a_i^\dagger a_i + \sum_i \alpha\nu \left(d_i^\dagger + d_i\right)\left(a_{i+1}^\dagger a_i + a_i^\dagger a_{i+1}\right) \end{aligned} \tag{51}$$

$b_{ik}/b_{ik}^\dagger$ stands for the intramolecular vibration with frequency ω_k and coupling constant g_k, which modifies the site energy. $d_i/d_i^\dagger$ is the intermolecular vibration with frequency ν and coupling constant α, which modifies the transfer integral V. At temperature T, the thermal fluctuation of the transfer integral due to intermolecular vibrations is $\Delta V = \alpha\nu\sqrt{\coth(\nu/2k_BT)}$. The charge mobility μ is calculated by TD-DMRG through the Kubo formula[161]:

$$\mu = \frac{1}{2k_BTe_0}\int_{-\infty}^{\infty} \left\langle \hat{j}(t)\hat{j}(0)\right\rangle_T dt, \tag{52}$$

where $\hat{j}$ is the charge current operator. The transfer integral of rubrene is 83 meV and the reorganization energy is 75 meV, indicating that rubrene is in the intermediate coupling regime. The frequency of intermolecular vibration is 50 cm^{-1}. Four to nine effective intramolecular modes in each molecule are considered depending on the parameter regime. The frequency and coupling constant of the vibrational modes and the other computational details can be found in References 77, 78.

Figure 14a shows the charge mobility with only intramolecular Holstein terms at room temperature calculated by TD-DMRG, FGR, and Boltzmann transport theory. In the weak electronic coupling regime, the numerical TD-DMRG results are consistent with the analytical FGR results (nonadiabatic limit). When V increases, FGR predicts a quadratic

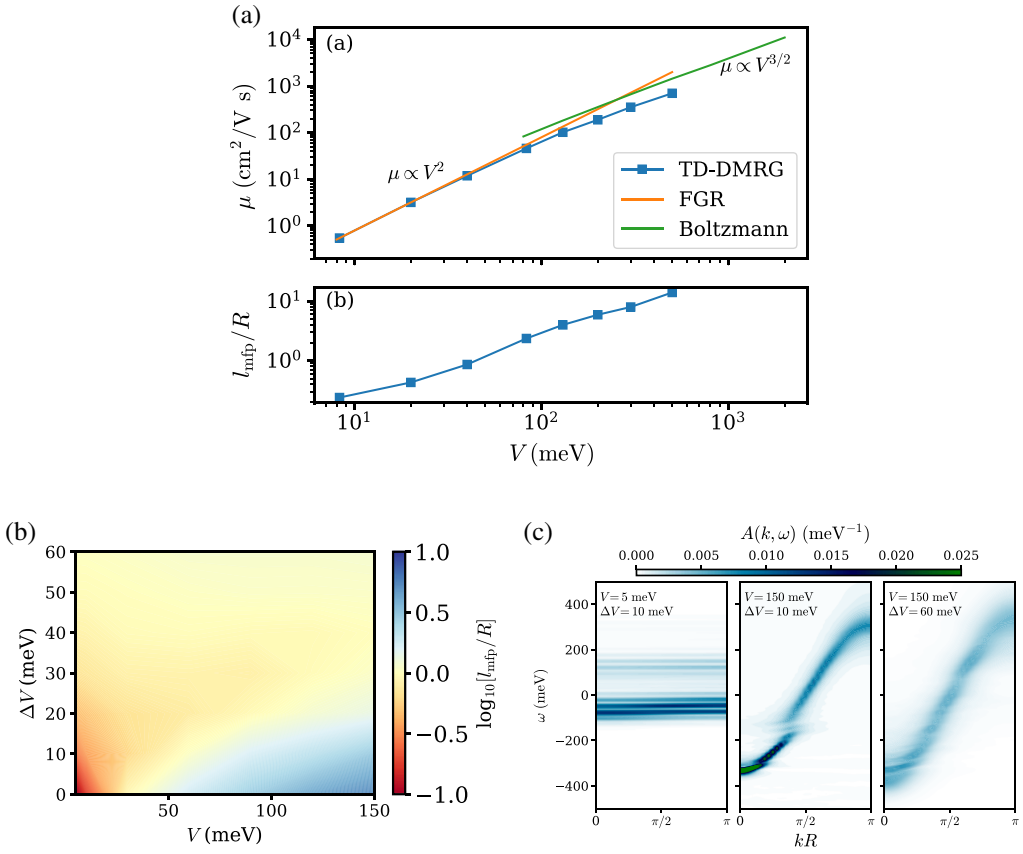

FIGURE 14 (a) Carrier mobility at 300 K from weak to strong electronic coupling V with only Holstein terms calculated by TD-DMRG, FGR (hopping limit), and Boltzmann transport theory (band limit). The lower panel is the corresponding mean free path l_{mfp} of the charge calculated by TD-DMRG. (b) Mean free path l_{mfp} for the Holstein-Peierls model at various transfer integral V and transfer integral thermal fluctuation ΔV calculated by TD-DMRG. (c) One-particle spectral function at 300 K for the Holstein–Peierls model calculated by TD-DMRG (adapted with permission from References 77,78)

increase in mobility, which will overestimate the mobility beyond the weak coupling regime compared to the TD-DMRG results. On the contrary, the Boltzmann transport theory can obtain correct mobility in the strong electronic coupling regime. Although this regime is very difficult for TD-DMRG, because a very long chain of molecules should be simulated for the mobility in the thermodynamic limit, the asymptotic behavior $\mu \propto V^{3/2}$ is correctly obtained. With the actual electronic coupling $V = 83$ meV of rubrene, both FGR and Boltzmann transport theory will overestimate the mobility. The mean free path ($l_{\mathrm{mfp}} = v\tau$) of the charge with the group velocity v and relaxation time τ can be estimated by[162]

$$\begin{aligned} v &= \sqrt{\left\langle \hat{j}(0)\hat{j}(0) \right\rangle}/e_0 \\ \tau &= \int_0^{\infty} \left| \frac{\mathrm{ReC(t)}}{\mathrm{ReC(0)}} \right| dt \end{aligned} \quad . \tag{53}$$

With only intramolecular Holstein terms, l_{mfp} is 2–3 in the actual parameter regime (the lower panel of Figure 14a). It means neither a fully localized hopping picture nor a fully delocalized band picture is valid. The problem becomes even more complicated when the intermolecular electron–phonon coupling terms are also considered. Figure 14b shows the mean free path of rubrene with respect to the electronic coupling V and its thermal fluctuation ΔV. From this 2-D contour, three distinct regimes can be identified: (i) In the left-bottom corner (both V and ΔV are small), the charge is mainly localized ($l_{\mathrm{mfp}} \ll 1$). Increasing the intermolecular electron–phonon coupling α will increase the mobility, called the phonon-assisted current. (ii) In the right-bottom corner (V is large while ΔV is small), the charge is quite

delocalized ($l_{\mathrm{mfp}} \gg 1$), which is the band-like regime. Increasing α will increase the phonon scattering and thus decrease the mobility. (iii) In the upper part of the figure (ΔV is large), the mean free path is close to 1 no matter how large V is, which corresponds to the transient localization regime.[163] We can gain more insight from the momentum resolved one-particle spectral function calculated by TD-DMRG.

$$A(k,\omega) = \frac{1}{N\pi}\sum_{mn}^{N} e^{ikR(m-n)} \int_0^\infty \left\langle a_m(t) a_n^\dagger(0)\right\rangle_T e^{i\omega t} dt. \tag{54}$$

In the phonon-assisted regime, the left panel of Figure 14c shows that there is no dispersion in the one-particle spectral function, indicating the charge is fully localized. The gap between the first and the second peaks is roughly 200 meV ($\sim$1600 cm^{-1}), which corresponds to the frequency of the highest intramolecular mode with prominent electron–phonon coupling constant g. In the band-like regime, the middle panel of Figure 14c shows a dispersive band and a sharp quasi-particle peak near $k \approx 0$, indicating the charge is delocalized. The resonance between the vibronic states opens up a small gap in the band. In the transient localization regime, though there is a quasi-particle band shown in the right panel of Figure 14c, the half-width of the spectral function is very wide (the band is "blurred"), indicating the lifetime of the delocalized quasi-particle is very short. This corresponds well to the picture of transient localization[163]: the delocalized charge is strongly affected by the intermolecular vibrations, which break the translational symmetry of the perfect crystal and thus lead to the charge localization. These three distinct regimes constitute a general charge transport picture for organic semiconductors with both intramolecular and intermolecular electron–phonon couplings, which can only be unified by the unbiased numerically exact method, such as TD-DMRG used here. For more detailed discussion, please refer to Reference 78.

4.2 | The radiationless decay rate of azulene molecule

TD-DMRG is not limited to harmonic vibrations and linear electron–vibration coupling. Recently, we applied it to calculate the radiationless decay rate of molecules beyond the common harmonic PES approximation.[81,82] The radiationless decay rate is one of the key quantities to predict the intrinsic luminescence quantum efficiency.[164] Unlike the radiative process, all the electronic excited energy needs to be received by the vibrations, which will be excited to high energy levels. Because the anharmonicity is probable to be very pronounced in the high-energy region of the PES far from the equilibrium position, the anharmonic effect should be considered for the radiationless process. In the weak nonadiabatic coupling regime where most luminescent molecules belong, the rate expression in the time domain under FGR is

$$k_{\mathrm{ic}} = \int_{-\infty}^{\infty} e^{i\Delta E_{\mathrm{ad}} t} C(t) dt. \tag{55}$$

$$C(t) = \left\langle \widehat{H}_1(t)\widehat{H}_1\right\rangle_T = \mathrm{Tr}\left(\frac{e^{-\beta\widehat{H}_{\mathrm{i}}}}{Z(\beta)} e^{i\widehat{H}_{\mathrm{i}}t}\widehat{H}_1 e^{-i\widehat{H}_{\mathrm{f}}t}\widehat{H}_1\right). \tag{56}$$

$\widehat{H}_{\mathrm{i}}$ and $\widehat{H}_{\mathrm{f}}$ are respectively the vibrational Hamiltonian of initial and final PES. ΔE_{ad} is the electronic adiabatic excitation energy. For internal conversion (IC), the perturbation operator $\widehat{H}_1$ is the nonadiabatic coupling operator. For intersystem crossing, $\widehat{H}_1$ is the spin–orbit coupling. The displacements, torsions (frequency difference), and rotations (mode-mixing) between the two PESs with respect to the corresponding normal coordinates are considered in the radiationless process.

$$q_{\mathrm{i},m} = \sum_l J_{ml} q_{\mathrm{f},l} + \Delta q_{\mathrm{i},m}. \tag{57}$$

In addition, the anharmonicity of the ground state PES is considered through the n-mode representation (n-MR) method.[112]

The S_1 to S_0 IC process of the azulene molecule is investigated. Azulene is the first experimentally discovered molecule exhibiting anti-Kasha rule luminescence (S_2 to S_0).[165,166] Its S_1 to S_0 IC rate is very fast, with experimental measurements of about 1–2 ps.[167] We calculate k_{ic} of azulene on anharmonic S_0 PES up to 2-MR. The 2-MR PES is expressed as

$$V(q_1,q_2,...,q_N)=V^{(0)}\left(\boldsymbol{q}^{\mathrm{ref}}\right)+\sum_i V^{(1)}\left(q_i;\boldsymbol{q}^{\mathrm{ref}}_{l\neq i}\right)+\sum_{i<j}V^{(2)}\left(q_i,q_j;\boldsymbol{q}^{\mathrm{ref}}_{l\neq ij}\right). \tag{58}$$

$$V^{(1)}\left(q_i;\boldsymbol{q}^{\mathrm{ref}}_{l\neq i}\right)=V\left(q_i;\boldsymbol{q}^{\mathrm{ref}}_{l\neq i}\right)-V^{(0)}\left(\boldsymbol{q}^{\mathrm{ref}}\right). \tag{59}$$

$$V^{(2)}\left(q_i,q_j;\boldsymbol{q}^{\mathrm{ref}}_{l\neq ij}\right)=V\left(q_i,q_j;\boldsymbol{q}^{\mathrm{ref}}_{l\neq ij}\right)-V^{(1)}\left(q_i;\boldsymbol{q}^{\mathrm{ref}}_{l\neq i}\right)-V^{(1)}\left(q_j;\boldsymbol{q}^{\mathrm{ref}}_{l\neq j}\right)-V^{(0)}\left(\boldsymbol{q}^{\mathrm{ref}}\right). \tag{60}$$

Equation (58) is an incremental expression, in which $V^{(0)}$ is the energy of the reference point (the equilibrium point of S_0 PES). The second terms $V^{(1)}$ and third terms $V^{(2)}$ are the incremental one-mode and two-mode potentials. $\left(q_i;\boldsymbol{q}^{\mathrm{ref}}_{l\neq i}\right)/\left(q_i;q_j;\boldsymbol{q}^{\mathrm{ref}}_{l\neq i}\right)$ indicates that only q_i/q_i, q_j can be different from the reference point. Each term in Equation (58) is fitted with a polynomial of order 12.[82] The results of k_{ic} are shown in Table 1. On harmonic (HA) PES, the numerical results of TD-DMRG can reproduce the analytically exact results of the thermal vibration correlation function method.[168] The rate on 1-MR PES is about 200% of the rate on HA PES, indicating that the introduction of intramode anharmonicity will prominently accelerate the rate of IC. More significantly, the coupling between modes has a greater effect on the IC rate: the rate on 2-MR PES is about 500% of the rate on HA PES. To some extent, this mode coupling effect is similar to the mode-mixing effect, both of which scramble the normal modes. This effect will accelerate the vibrational relaxation and thus the dephasing of the wavepackets on the excited and ground state PESs.

Furthermore, we examine the magnitude of the anharmonic effect with different energy gaps. Figure 15a plots k_{ic} on HA, 1-MR, and 2-MR PESs at 0 and 300 K with different adiabatic energy gaps ΔE_{ad}. It shows that the magnitude of the energy gap is very important for the anharmonicity to take effect. With a gap smaller than 1.6 eV, there is basically no anharmonic effect. With the increase of the gap, the anharmonic effect becomes more and more noticeable. The IC rate on HA PES decreases much faster than that on anharmonic 1-/2-MR PES with the increase of gap. This behavior, which has also been reported in the study of model molecules,[169] is due to that the larger the gap, the higher the energy level of the final vibrational state, and therefore the greater the anharmonic effect.

The final-state-resolved IC rates $k_{v_1v_2\cdots v_N}$ (the final vibrational state is labeled as $v_1v_2\cdots v_N$) for the HA and 1-MR PESs are also calculated by TD-DMRG. Based on that, the mean vibrational quantum number and the mean accepting energy for each mode can be defined as $\bar{v}_l=\sum_{v_l}p_{v_l}v_l$, $\bar{\epsilon}_l=\sum_{v_l}p_{v_l}\epsilon_{v_l}$, where ϵ_{v_l} is the energy of vibrational state v_l. $p_{v_l}=\sum_{\text{all } v_{k,k\neq l}}\frac{k_{v_1v_2,\ldots,v_l,\ldots,v_N}}{k_{ic}}$. $\bar{v}_l$ on different PESs are shown in Figure 15b (black for 0 K, red for 300 K), in which the total $\bar{\epsilon}_l$ of the 8 high-frequency C–H vibrations above 3000 cm^{-1} ($\sum\bar{\epsilon}_{C-H}$) are also listed. For HA PES (upper panel), the modes with large Huang–Rhys (HR) factors receive more energy and the corresponding $\bar{v}_l$ is larger. The main contributor, mode 38, has the largest 2.7 mean vibrational quantum number, while the high-frequency C–H vibrations with small HR factors basically do not contribute, with a mean accepting energy of 1098 cm^{-1} (0 K)/1090 cm^{-1} (300 K). For 1-MR

TABLE 1 The internal conversion rate k_{ic} of azulene from S_1 to S_0 with harmonic PES, anharmonic 1-MR, and 2-MR PESs calculated by TD-DMRG

	k_{ic} ($\times10^{10}$ s^{-1}) at 0 K			k_{ic} ($\times10^{10}$ s^{-1}) at 300 K		
Method	**HA**	**1-MR**	**2-MR**	**HA**	**1-MR**	**2-MR**
TVCF	0.79	—	—	1.00	—	—
TD-DMRG	0.79	1.47 (186%)	3.56 (451%)	0.97	1.86 (192%)	4.53 (467%)

Note: The analytically exact results with harmonic PES calculated by TVCF are also listed. A 100 cm^{-1} Gaussian broadening is applied. The values in parentheses are relative to HA (adapted with permission from Reference 82).

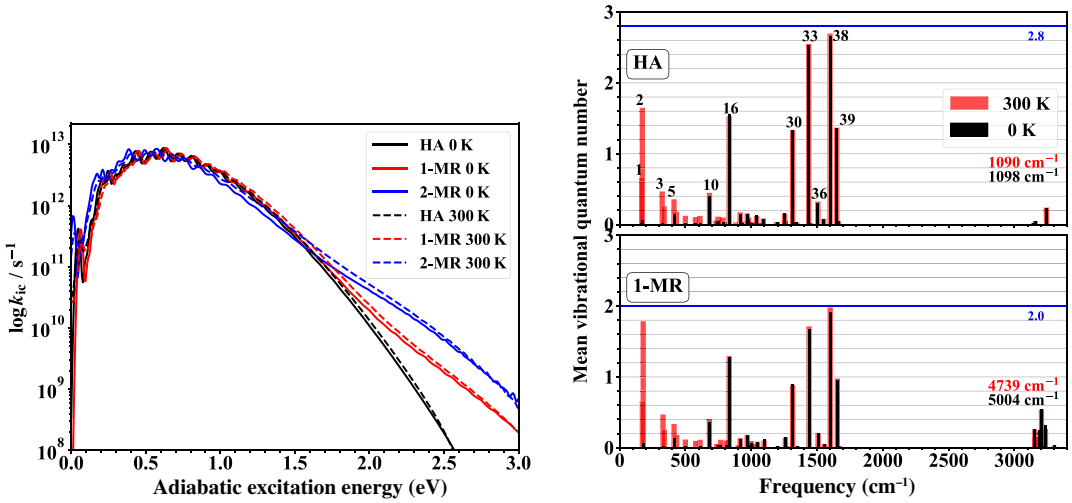

FIGURE 15 (a) k_{ic} of azulene on the HA (black), 1-MR (red), and 2-MR (blue) PESs at different S_0, S_1 adiabatic energy gaps. Solid line is $T = 0$ K, dashed line is $T = 300$ K. (b) The mean vibrational quantum number $\bar{v}_l$ received by each mode on the HA and 1-MR ground state PESs. The black is for 0 K and the red is for 300 K. The total mean accepting energy $\sum \bar{\epsilon}_{C-H}$ of the C–H vibrations is also listed. The horizontal blue line is a guide to the eye (reprinted with permission from Reference 82)

PES (lower panel), $\bar{v}_l$ in the C–C vibrational region decreases significantly, with the largest (mode 38) being 2.0. This is mainly due to the significantly enhanced contribution of C–H vibrations, whose mean accepting energy is increased to 5004 cm^{-1} (0 K)/4739 cm^{-1} (300 K). Therefore, by considering anharmonicity, the ability of C–H vibrations to receive electronic energy is opened up. Since the C–H vibrations receive more energy, the quantum numbers of the C–C vibrations decrease. Qualitatively, according to that the Franck–Condon (FC) factor between two displaced harmonic oscillators is $|\langle\chi_{i0}|\chi_{fv}\rangle|^2 = \frac{e^{-S}S^v}{v!}$ and for azulene HR factors S are less than 1 (weak coupling regime), smaller v results in a larger FC factor and thus a faster IC rate after accounting for anharmonicity. Given that the C–H vibrations are quite local, we expect this anharmonic effect on radiationless decay rate to be prevalent in small to medium-sized hydrocarbon compounds.

5 | CONCLUSION AND OUTLOOK

TD-DMRG is a very powerful method for studying the quantum dynamics of high-dimensional systems. It has the advantages of high accuracy, efficiency, and robustness. In this review, we start from the introduction of MPS and MPO that are the cornerstones of modern TD-DMRG theory. For MPS, the tangent space is introduced, which is very important in time-dependent theory and post-MPS theories. For MPO, we introduce the recently developed automated MPO construction algorithm, which enables TD-DMRG to be more easily extended to different dynamical problems. Based on MPS and MPO, a variety of newly developed time evolution schemes provide effective tools to achieve accurate time evolution of complex many-body systems, among which the scheme based on TDVP is the most efficient and accurate one in our experience. Although TD-DMRG is essentially a wavefunction theory, based on the ITE method or the TFD method, TD-DMRG can also obtain thermal equilibrium states, which can be further combined with real-time evolution to deal with dynamical problems at finite temperature. Due to the presence of a large number of tensor contractions in the TD-DMRG algorithm, GPU can accelerate TD-DMRG by tens of times, enabling TD-DMRG to handle hundreds to thousands of DoFs. We show the accuracy of TD-DMRG by comparing it with other highly accurate methods in simulating the dynamics of the SBM and Frenkel–Holstein models, and analyze its computational scaling in detail. The selected applications include the dynamics of molecular aggregates in the condensed phase and single molecular dynamics in the gas phase, demonstrating the universality of TD-DMRG in dealing with high-dimensional electron-vibration coupled problems.

However, there are also some limitations and challenges in TD-DMRG. The difficulty for dealing with condensed phase problems lies in that very large computational effort is spent on treating the environment as a closed system together, even though the information about the environment is of less interest. The recent idea of combining the reduced dynamics theory and TD-DMRG provides new opportunities in this direction.[86,87,140] The difficulty for dealing with molecular problems lies in how to represent the global PES of a real molecule into a SOP form that TD-DMRG can handle. This is still an open question so far for medium-sized molecules. To bypass this problem, another direction is to formulate TD-DMRG as an on-the-fly approach, which deserves further study.

ACKNOWLEDGMENTS

We gratefully thank Yaming Yan, Meng Xu, and Qiang Shi for providing the reference data. We thank Hans-Dieter Meyer for providing the Heidelberg ML-MCTDH package. This work is supported by the National Natural Science Foundation of China (NSFC) through the project "Science CEnter for Luminescence from Molecular Aggregates (SCELMA)" Grant Number 21788102 and through Grant Number 22003029, as well as by the Ministry of Science and Technology of China through the National Key R&D Plan Grant Number 2017YFA0204501.

CONFLICT OF INTEREST

The authors have declared no conflicts of interest for this article.

DATA AVAILABILITY STATEMENT

The data that support the findings of this study are available from the corresponding author upon reasonable request.

AUTHOR CONTRIBUTIONS

Jiajun Ren: Conceptualization (equal); writing – original draft (equal); writing – review and editing (equal). **Weitang Li:** Writing – original draft (equal); writing – review and editing (equal). **Tong Jiang:** Writing – review and editing (equal). **Yuanheng Wang:** Writing – review and editing (equal). **Zhigang Shuai:** Conceptualization (equal); supervision (equal); writing – original draft (equal); writing – review and editing (equal).

ORCID

Jiajun Ren https://orcid.org/0000-0002-1508-4943
Zhigang Shuai https://orcid.org/0000-0003-3867-2331

RELATED WIREs ARTICLE

Finite temperature quantum dynamics of complex systems: Integrating thermo-field theories and tensor-train methods

REFERENCES

1. Cheng YC, Fleming GR. Dynamics of light harvesting in photosynthesis. Annu Rev Phys Chem. 2009;60:241–62.
2. Mirkovic T, Ostroumov EE, Anna JM, Van Grondelle R, Scholes GD. Light absorption and energy transfer in the antenna complexes of photosynthetic organisms. Chem Rev. 2017;117(2):249–93.
3. Brédas JL, Norton JE, Cornil J, Coropceanu V. Molecular understanding of organic solar cells: the challenges. Acc Chem Res. 2009;42(11):1691–9.
4. Troisi A. Charge transport in high mobility molecular semiconductors: classical models and new theories. Chem Soc Rev. 2011;40(5):2347–58.
5. Shuai Z, Geng H, Xu W, Liao Y, André JM. From charge transport parameters to charge mobility in organic semiconductors through multiscale simulation. Chem Soc Rev. 2014;43(8):2662–79.
6. Schröter M, Ivanov SD, Schulze J, Polyutov SP, Yan Y, Pullerits T, et al. Exciton–vibrational coupling in the dynamics and spectroscopy of Frenkel excitons in molecular aggregates. Phys Rep. 2015;567:1–78.
7. Leggett AJ, Chakravarty S, Dorsey AT, Fisher MP, Garg A, Zwerger W. Dynamics of the dissipative two-state system. Rev Mod Phys. 1987;59(1):1.
8. May V, Kühn O. Charge and energy transfer dynamics in molecular systems. Weinheim: John Wiley & Sons; 2008.
9. Mukamel S. Principles of nonlinear optical spectroscopy. New York: Oxford University Press; 1995.
10. Crespo-Otero R, Barbatti M. Recent advances and perspectives on nonadiabatic mixed quantum–classical dynamics. Chem Rev. 2018;118(15):7026–68.
11. Curchod BF, Martínez TJ. Ab initio nonadiabatic quantum molecular dynamics. Chem Rev. 2018;118(7):3305–36.
12. González L, Lindh R. Quantum chemistry and dynamics of excited states: methods and applications. West Sussex: John Wiley & Sons; 2020.

13. Habershon S, Manolopoulos DE, Markland TE, Miller TF III. Ring-polymer molecular dynamics: quantum effects in chemical dynamics from classical trajectories in an extended phase space. Annu Rev Phys Chem. 2013;64:387–413.
14. Liu J, He X, Wu B. Unified formulation of phase space mapping approaches for nonadiabatic quantum dynamics. Acc Chem Res. 2021; 54:4215–28.
15. Wang L, Qiu J, Bai X, Xu J. Surface hopping methods for nonadiabatic dynamics in extended systems. WIREs Comput Mol Sci. 2020; 10(2):e1435.
16. Feit M, Fleck J Jr, Steiger A. Solution of the Schrödinger equation by a spectral method. J Comput Phys. 1982;47(3):412–33.
17. Park TJ, Light J. Unitary quantum time evolution by iterative Lanczos reduction. J Chem Phys. 1986;85(10):5870–6.
18. Tal-Ezer H, Kosloff R. An accurate and efficient scheme for propagating the time dependent Schrödinger equation. J Chem Phys. 1984; 81(9):3967–71.
19. Meyer HD, Manthe U, Cederbaum LS. The multi-configurational time-dependent Hartree approach. Chem Phys Lett. 1990;165(1): 73–8.
20. Wang H, Thoss M. Multilayer formulation of the multiconfiguration time-dependent Hartree theory. J Chem Phys. 2003;119(3): 1289–99.
21. Beck MH, Jäckle A, Worth GA, Meyer HD. The multiconfiguration time-dependent Hartree (MCTDH) method: a highly efficient algorithm for propagating wavepackets. Phys Rep. 2000;324(1):1–105.
22. Wang H, Thoss M. From coherent motion to localization: dynamics of the spin-boson model at zero temperature. New J Phys. 2008; 10(11):115005.
23. Wang H, Thoss M. From coherent motion to localization: II. Dynamics of the spin-boson model with sub-Ohmic spectral density at zero temperature. Chem Phys. 2010;370(1–3):78–86.
24. Tanimura Y, Kubo R. Time evolution of a quantum system in contact with a nearly Gaussian-Markoffian noise bath. J Phys Soc Jpn. 1989;58(1):101–14.
25. Yan Y, Yang F, Liu Y, Shao J. Hierarchical approach based on stochastic decoupling to dissipative systems. Chem Phys Lett. 2004; 395(4–6):216–21.
26. Tanimura Y. Numerically "exact" approach to open quantum dynamics: the hierarchical equations of motion (HEOM). J Chem Phys. 2020;153(2):020901.
27. Ye L, Wang X, Hou D, Xu RX, Zheng X, Yan Y. HEOM-QUICK : a program for accurate, efficient, and universal characterization of strongly correlated quantum impurity systems. WIREs Computational Molecular Science. 2016;6(6):608–38. http://dx.doi.org/10.1002/wcms.1269
28. Makri N, Makarov DE. Tensor propagator for iterative quantum time evolution of reduced density matrices. I. Thoery. J Chem Phys. 1995;102(11):4600–10.
29. Makri N, Makarov DE. Tensor propagator for iterative quantum time evolution of reduced density matrices. II. Numerical methodology. J Chem Phys. 1995;102(11):4611–8.
30. Strunz WT, Diósi L, Gisin N. Open system dynamics with non-Markovian quantum trajectories. Phys Rev Lett. 1999;82(9):1801.
31. Suess D, Eisfeld A, Strunz W. Hierarchy of stochastic pure states for open quantum system dynamics. Phys Rev Lett. 2014;113(15): 150403.
32. Shi Q, Geva E. A new approach to calculating the memory kernel of the generalized quantum master equation for an arbitrary system–bath coupling. J Chem Phys. 2003;119(23):12063–76.
33. Mulvihill E, Geva E. A road map to various pathways for calculating the memory kernel of the generalized quantum master equation. J Phys Chem B. 2021;125(34):9834–52.
34. Ma H, Luo Z, Yao Y. The time-dependent density matrix renormalisation group method. Mol Phys. 2018;116(7–8):854–68.
35. White SR. Density matrix formulation for quantum renormalization groups. Phys Rev Lett. 1992;69(19):2863.
36. White SR. Density-matrix algorithms for quantum renormalization groups. Phys Rev B. 1993;48(14):10345.
37. Shuai Z, Brédas JL, Pati SK, Ramasesha S. Quantum confinement effects on the ordering of the lowest-lying excited states in conjugated polymers. Proc SPIE Int Soc Opt Eng. 1997;3145:293–302.
38. Fano G, Ortolani F, Ziosi L. The density matrix renormalization group method: application to the PPP model of a cyclic polyene chain. J Chem Phys. 1998;108(22):9246–52.
39. White SR, Martin RL. Ab initio quantum chemistry using the density matrix renormalization group. J Chem Phys. 1999;110(9): 4127–30.
40. Chan GKL, Sharma S. The density matrix renormalization group in quantum chemistry. Annu Rev Phys Chem. 2011;62:465–81.
41. Rakhuba M, Oseledets I. Calculating vibrational spectra of molecules using tensor train decomposition. J Chem Phys. 2016;145(12): 124101.
42. Baiardi A, Stein CJ, Barone V, Reiher M. Vibrational density matrix renormalization group. J Chem Theory Comput. 2017;13(8): 3764–77.
43. Baiardi A, Stein CJ, Barone V, Reiher M. Optimization of highly excited matrix product states with an application to vibrational spectroscopy. J Chem Phys. 2019;150(9):094113.
44. Ren J, Li W, Jiang T, Shuai Z. A general automatic method for optimal construction of matrix product operators using bipartite graph theory. J Chem Phys. 2020;153(8):084118.
45. Vidal G. Efficient simulation of one-dimensional quantum many-body systems. Phys Rev Lett. 2004;93(4):040502.

46. Stoudenmire E, White SR. Minimally entangled typical thermal state algorithms. New J Phys. 2010;12(5):055026.
47. White SR, Feiguin AE. Real-time evolution using the density matrix renormalization group. Phys Rev Lett. 2004;93(7):076401.
48. Daley AJ, Kollath C, Schollwöck U, Vidal G. Time-dependent density-matrix renormalization-group using adaptive effective Hilbert spaces. J Stat Mech Theory Exp. 2004;2004(04):P04005.
49. Östlund S, Rommer S. Thermodynamic limit of density matrix renormalization. Phys Rev Lett. 1995;75(19):3537.
50. Schollwöck U. The density-matrix renormalization group in the age of matrix product states. Ann Phys. 2011;326(1):96–192.
51. Crosswhite GM, Bacon D. Finite automata for caching in matrix product algorithms. Phys Rev A. 2008;78(1):012356.
52. Keller S, Dolfi M, Troyer M, Reiher M. An efficient matrix product operator representation of the quantum chemical Hamiltonian. J Chem Phys. 2015;143(24):244118.
53. Chan GKL, Keselman A, Nakatani N, Li Z, White SR. Matrix product operators, matrix product states, and ab initio density matrix renormalization group algorithms. J Chem Phys. 2016;145(1):014102.
54. Hubig C, McCulloch I, Schollwöck U. Generic construction of efficient matrix product operators. Phys Rev B. 2017;95(3):035129.
55. García-Ripoll JJ. Time evolution of matrix product states. New J Phys. 2006;8(12):305.
56. Wall M, Carr LD. Out-of-equilibrium dynamics with matrix product states. New J Phys. 2012;14(12):125015.
57. Zaletel MP, Mong RS, Karrasch C, Moore JE, Pollmann F. Time-evolving a matrix product state with long-ranged interactions. Phys Rev B. 2015;91(16):165112.
58. Greene SM, Batista VS. Tensor-train split-operator Fourier transform (TT-SOFT) method: multidimensional nonadiabatic quantum dynamics. J Chem Theory Comput. 2017;13(9):4034–42.
59. Ren J, Shuai Z, Kin-Lic CG. Time-dependent density matrix renormalization group algorithms for nearly exact absorption and fluorescence spectra of molecular aggregates at both zero and finite temperature. J Chem Theory Comput. 2018;14(10):5027–39.
60. Haegeman J, Cirac JI, Osborne TJ, Pižorn I, Verschelde H, Verstraete F. Time-dependent variational principle for quantum lattices. Phys Rev Lett. 2011;107(7):070601.
61. Lubich C, Oseledets IV, Vandereycken B. Time integration of tensor trains. SIAM J Numer Anal. 2015;53(2):917–41.
62. Haegeman J, Lubich C, Oseledets I, Vandereycken B, Verstraete F. Unifying time evolution and optimization with matrix product states. Phys Rev B. 2016;94(16):165116.
63. Baiardi A, Reiher M. Large-scale quantum dynamics with matrix product states. J Chem Theory Comput. 2019;15(6):3481–98.
64. Li W, Ren J, Shuai Z. Numerical assessment for accuracy and GPU acceleration of TD-DMRG time evolution schemes. J Chem Phys. 2020;152(2):024127.
65. Nakatani N, Chan GKL. Efficient tree tensor network states (TTNS) for quantum chemistry: generalizations of the density matrix renormalization group algorithm. J Chem Phys. 2013;138(13):134113.
66. Gunst K, Verstraete F, Wouters S, Legeza O, Van Neck D. T3NS: three-legged tree tensor network states. J Chem Theory Comput. 2018;14(4):2026–33.
67. Orús R. A practical introduction to tensor networks: matrix product states and projected entangled pair states. Ann Phys. 2014;349:117–58.
68. Larsson HR. Computing vibrational eigenstates with tree tensor network states (TTNS). J Chem Phys. 2019;151(20):204102.
69. Baiardi A, Reiher M. The density matrix renormalization group in chemistry and molecular physics: recent developments and new challenges. J Chem Phys. 2020;152(4):040903.
70. Prior J, Chin AW, Huelga SF, Plenio MB. Efficient simulation of strong system-environment interactions. Phys Rev Lett. 2010;105(5):050404.
71. Chin A, Prior J, Rosenbach R, Caycedo-Soler F, Huelga SF, Plenio MB. The role of non-equilibrium vibrational structures in electronic coherence and recoherence in pigment–protein complexes. Nat Phys. 2013;9(2):113–8.
72. Yao Y. Polaronic quantum diffusion in dynamic localization regime. New J Phys. 2017;19(4):043015.
73. Borrelli R, Gelin MF. Simulation of quantum dynamics of excitonic systems at finite temperature: an efficient method based on thermo field dynamics. Sci Rep. 2017;7(1):1–9.
74. Kloss B, Reichman DR, Tempelaar R. Multiset matrix product state calculations reveal mobile Franck–Condon excitations under strong Holstein-type coupling. Phys Rev Lett. 2019;123(12):126601.
75. Yao Y, Xie X, Ma H. Ultrafast long-range charge separation in organic photovoltaics: promotion by off-diagonal vibronic couplings and entropy increase. J Phys Chem Lett. 2016;7(23):4830–5.
76. Yao Y, Sun KW, Luo Z, Ma H. Full quantum dynamics simulation of a realistic molecular system using the adaptive time-dependent density matrix renormalization group method. J Phys Chem Lett. 2018;9(2):413–9.
77. Li W, Ren J, Shuai Z. Finite-temperature TD-DMRG for the carrier mobility of organic semiconductors. J Phys Chem Lett. 2020;11(13):4930–6.
78. Li W, Ren J, Shuai Z. A general charge transport picture for organic semiconductors with nonlocal electron-phonon couplings. Nat Commun. 2021;12(1):1–9.
79. Schröder FA, Turban DH, Musser AJ, Hine ND, Chin AW. Tensor network simulation of multi-environmental open quantum dynamics via machine learning and entanglement renormalisation. Nat Commun. 2019;10(1):1–10.
80. Xie X, Liu Y, Yao Y, Schollwöck U, Liu C, Ma H. Time-dependent density matrix renormalization group quantum dynamics for realistic chemical systems. J Chem Phys. 2019;151(22):224101.

81. Wang Y, Ren J, Shuai Z. Evaluating the anharmonicity contributions to the molecular excited state internal conversion rates with finite temperature TD-DMRG. J Chem Phys. 2021;154(21):214109.
82. Ren J, Wang Y, Li W, Jiang T, Shuai Z. TD-DMRG coupled with n-mode representation potentials for the excited state radiationless decay rate: formalism and application to azulene. Chin J Chem Phys. 2021;34(5):565–82.
83. Ronca E, Li Z, Jimenez-Hoyos CA, Chan GKL. Time-step targeting time-dependent and dynamical density matrix renormalization group algorithms with ab initio Hamiltonians. J Chem Theory Comput. 2017;13(11):5560–71.
84. Frahm LH, Pfannkuche D. Ultrafast ab initio quantum chemistry using matrix product states. J Chem Theory Comput. 2019;15(4):2154–65.
85. Baiardi A. Electron Dynamics with the Time-Dependent Density Matrix Renormalization Group. J Chem Theory Comput. 2021;17(6):3320–34. http://dx.doi.org/10.1021/acs.jctc.0c01048
86. Shi Q, Xu Y, Yan Y, Xu M. Efficient propagation of the hierarchical equations of motion using the matrix product state method. J Chem Phys. 2018;148(17):174102.
87. Flannigan S, Damanet F, Daley AJ. Many-body quantum state diffusion for non-Markovian dynamics in strongly interacting systems. Phys Rev Lett. 2022;128(6):063601.
88. Strathearn A, Kirton P, Kilda D, Keeling J, Lovett BW. Efficient non-Markovian quantum dynamics using time-evolving matrix product operators. Nat Commun. 2018;9(1):1–9.
89. Oseledets IV. Tensor-train decomposition. SIAM J Sci Comput. 2011;33(5):2295–317.
90. Light JC, Carrington T Jr. Discrete-variable representations and their utilization. Adv Chem Phys. 2000;114:263–310.
91. Paeckel S, Köhler T, Swoboda A, Manmana SR, Schollwöck U, Hubig C. Time-evolution methods for matrix-product states. Ann Phys. 2019;411:167998.
92. Eisert J, Cramer M, Plenio MB. Colloquium: area laws for the entanglement entropy. Rev Mod Phys. 2010;82(1):277.
93. Gobert D, Kollath C, Schollwöck U, Schütz G. Real-time dynamics in spin-1/2 chains with adaptive time-dependent density matrix renormalization group. Phys Rev E. 2005;71(3):036102.
94. De Chiara G, Montangero S, Calabrese P, Fazio R. Entanglement entropy dynamics of Heisenberg chains. J Stat Mech Theory Exp. 2006;2006(03):P03001.
95. Haegeman J, Osborne TJ, Verstraete F. Post-matrix product state methods: to tangent space and beyond. Phys Rev B. 2013;88(7):075133.
96. Kinder JM, Ralph CC, Kin-Lic CG. Analytic time evolution, random phase approximation, and green functions for matrix product states. Quantum. Inf Comput. 2014;154:179–191.
97. Wouters S, Nakatani N, Van Neck D, Chan GKL. Thouless theorem for matrix product states and subsequent post density matrix renormalization group methods. Phys Rev B. 2013;88(7):075122.
98. Nakatani N, Wouters S, Van Neck D, Chan GKL. Linear response theory for the density matrix renormalization group: efficient algorithms for strongly correlated excited states. J Chem Phys. 2014;140(2):024108.
99. Li Z, Chan GKL. Spin-projected matrix product states: versatile tool for strongly correlated systems. J Chem Theory Comput. 2017;13(6):2681–95.
100. Jiang T, Ren J, Shuai Z. Chebyshev matrix product states with canonical orthogonalization for spectral functions of many-body systems. J Phys Chem Lett. 2021;12:9344–52.
101. Jeckelmann E. Dynamical density-matrix renormalization-group method. Phys Rev B. 2002;66(4):045114.
102. Jiang T, Li W, Ren J, Shuai Z. Finite temperature dynamical density matrix renormalization group for spectroscopy in frequency domain. J Phys Chem Lett. 2020;11(10):3761–8.
103. McCulloch IP. From density-matrix renormalization group to matrix product states. J Stat Mech Theory Exp. 2007;2007(10):P10014.
104. Xiang T. Density-matrix renormalization-group method in momentum space. Phys Rev B. 1996;53(16):R10445.
105. Bondy JA, Murty USR. Graph theory with applications. Vol 290. London: Macmillan; 1976.
106. Kuhn HW. The Hungarian method for the assignment problem. Nav Res Logist. 1955;2(1–2):83–97.
107. Hopcroft JE, Karp RM. An $n^{5/2}$ algorithm for maximum matchings in bipartite graphs. SIAM J Comput. 1973;2(4):225–31.
108. Jäckle A, Meyer HD. Product representation of potential energy surfaces. J Chem Phys. 1996;104(20):7974–84.
109. Peláez D, Meyer HD. The multigrid POTFIT (MGPF) method: grid representations of potentials for quantum dynamics of large systems. J Chem Phys. 2013;138(1):014108.
110. Manzhos S, Carrington T Jr. Using neural networks to represent potential surfaces as sums of products. J Chem Phys. 2006;125(19):194105.
111. Manzhos S, Dawes R, Carrington T. Neural network-based approaches for building high dimensional and quantum dynamics-friendly potential energy surfaces. Int J Quantum Chem. 2015;115(16):1012–20.
112. Li G, Rosenthal C, Rabitz H. High dimensional model representations. J Phys Chem A. 2001;105(33):7765–77.
113. Klinting EL, Thomsen B, Godtliebsen IH, Christiansen O. Employing general fit-bases for construction of potential energy surfaces with an adaptive density-guided approach. J Chem Phys. 2018;148(6):064113.
114. Vendrell O, Gatti F, Lauvergnat D, Meyer HD. Full-dimensional (15-dimensional) quantum-dynamical simulation of the protonated water dimer. I. Hamiltonian setup and analysis of the ground vibrational state. J Chem Phys. 2007;127(18):184302.
115. Halimeh JC, Kolley F, McCulloch IP. Chebyshev matrix product state approach for time evolution. Phys Rev B. 2015;92(11):115130.

116. Dirac PA. Note on exchange phenomena in the Thomas atom. Mathematical proceedings of the Cambridge Philosophical Society. Volume 26. Cambridge: Cambridge University Press; 1930. p. 376–85.
117. Feiguin AE, White SR. Time-step targeting methods for real-time dynamics using the density matrix renormalization group. Phys Rev B. 2005;72(2):020404.
118. Chin AW, Rivas Á, Huelga SF, Plenio MB. Exact mapping between system-reservoir quantum models and semi-infinite discrete chains using orthogonal polynomials. J Math Phys. 2010;51(9):092109.
119. Sauer T. Numerical analysis. 2nd ed. Upper Saddle River: George Mason University. Pearson Education Inc; 2012.
120. Gatti F, Lasorne B, Meyer HD, Nauts A. Applications of quantum dynamics in chemistry. Vol 98. Cham: Springer; 2017.
121. Meyer HD, Wang H. On regularizing the MCTDH equations of motion. J Chem Phys. 2018;148(12):124105.
122. Wang H, Meyer HD. On regularizing the ML-MCTDH equations of motion. J Chem Phys. 2018;149(4):044119.
123. Yang M, White SR. Time-dependent variational principle with ancillary Krylov subspace. Phys Rev B. 2020;102(9):094315.
124. Dunnett AJ, Chin AW. Efficient bond-adaptive approach for finite-temperature open quantum dynamics using the one-site time-dependent variational principle for matrix product states. Phys Rev B. 2021;104(21):214302.
125. Xu Y, Xie Z, Xie X, Schollwöck U, Ma H. Stochastic adaptive single-site time-dependent variational principle. JACS Au. 2022;2(2):335–40. https://doi.org/10.1021/jacsau.1c00474
126. Kloss B, Burghardt I, Lubich C. Implementation of a novel projector-splitting integrator for the multi-configurational time-dependent Hartree approach. J Chem Phys. 2017;146(17):174107.
127. Feiguin AE, White SR. Finite-temperature density matrix renormalization using an enlarged Hilbert space. Phys Rev B. 2005;72(22):220401.
128. Takahashi Y, Umezawa H. Thermo field dynamics. Int J Mod Phys B. 1996;10(13n14):1755–805.
129. Borrelli R, Gelin MF. Quantum electron-vibrational dynamics at finite temperature: thermo field dynamics approach. J Chem Phys. 2016;145(22):224101.
130. de Vega I, Banuls MC. Thermofield-based chain-mapping approach for open quantum systems. Phys Rev A. 2015;92(5):052116.
131. Borrelli R, Gelin MF. Finite temperature quantum dynamics of complex systems: integrating thermo-field theories and tensor-train methods. WIREs Comput Mol Sci. 2021;11(6):e1539.
132. Steeb WH, Hardy Y. Bose, spin and Fermi systems: problems and solutions. Singapore: World Scientific Publishing Company; 2015.
133. Tamascelli D, Smirne A, Lim J, Huelga SF, Plenio MB. Efficient simulation of finite-temperature open quantum systems. Phys Rev Lett. 2019;123(9):090402.
134. Suzuki M. Density matrix formalism, double-space and thermo field dynamics in non-equilibrium dissipative systems. Int J Mod Phys B. 1991;5(11):1821–42.
135. Barthel T. Precise evaluation of thermal response functions by optimized density matrix renormalization group schemes. New J Phys. 2013;15(7):073010.
136. Verstraete F, Garcia-Ripoll JJ, Cirac JI. Matrix product density operators: simulation of finite-temperature and dissipative systems. Phys Rev Lett. 2004;93(20):207204.
137. Zwolak M, Vidal G. Mixed-state dynamics in one-dimensional quantum lattice systems: a time-dependent superoperator renormalization algorithm. Phys Rev Lett. 2004;93(20):207205.
138. Karrasch C, Bardarson J, Moore J. Finite-temperature dynamical density matrix renormalization group and the Drude weight of spin-1/2 chains. Phys Rev Lett. 2012;108(22):227206.
139. Yan Y, Xing T, Shi Q. A new method to improve the numerical stability of the hierarchical equations of motion for discrete harmonic oscillator modes. J Chem Phys. 2020;153(20):204109.
140. Yan Y, Xu M, Li T, Shi Q. Efficient propagation of the hierarchical equations of motion using the Tucker and hierarchical Tucker tensors. J Chem Phys. 2021;154(19):194104.
141. Borrelli R. Density matrix dynamics in twin-formulation: an efficient methodology based on tensor-train representation of reduced equations of motion. J Chem Phys. 2019;150(23):234102.
142. Fang JY, Guo H. Multiconfiguration time-dependent Hartree studies of the CH_3I/MgO photodissociation dynamics. J Chem Phys. 1994;101(7):5831–40.
143. Legeza Ö, Sólyom J. Optimizing the density-matrix renormalization group method using quantum information entropy. Phys Rev B. 2003;68(19):195116.
144. Moritz G, Hess BA, Reiher M. Convergence behavior of the density-matrix renormalization group algorithm for optimized orbital orderings. J Chem Phys. 2005;122(2):024107.
145. Rissler J, Noack RM, White SR. Measuring orbital interaction using quantum information theory. Chem Phys. 2006;323(2–3):519–31.
146. Olivares-Amaya R, Hu W, Nakatani N, Sharma S, Yang J, Chan GKL. The ab-initio density matrix renormalization group in practice. J Chem Phys. 2015;142(3):034102.
147. Krumnow C, Veis L, Legeza Ö, Eisert J. Fermionic orbital optimization in tensor network states. Phys Rev Lett. 2016;117(21):210402.
148. Kurashige Y. Matrix product state formulation of the multiconfiguration time-dependent Hartree theory. J Chem Phys. 2018;149(19):194114.
149. Guo C, Weichselbaum A, von Delft J, Vojta M. Critical and strong-coupling phases in one-and two-bath spin-boson models. Phys Rev Lett. 2012;108(16):160401.

150. Li Z. Expressibility of comb tensor network states (CTNS) for the P-cluster and the FeMo-cofactor of nitrogenase. Electron Struct. 2021; 3(1):014001.
151. Schröder FA, Chin AW. Simulating open quantum dynamics with time-dependent variational matrix product states: towards microscopic correlation of environment dynamics and reduced system evolution. Phys Rev B. 2016;93(7):075105.
152. Renormalizer. https://github.com/shuaigroup/Renormalizer.
153. Mainali S, Gatti F, Iouchtchenko D, Roy PN, Meyer HD. Comparison of the multi-layer multi-configuration time-dependent Hartree (ML-MCTDH) method and the density matrix renormalization group (DMRG) for ground state properties of linear rotor chains. J Chem Phys. 2021;154(17):174106.
154. Vendrell O, Meyer HD. The MCTDH Package, version 8.5; 2021. http://mctdh.uni-hd.de.
155. Engel GS, Calhoun TR, Read EL, Ahn TK, Mančal T, Cheng YC, et al. Evidence for wavelike energy transfer through quantum coherence in photosynthetic systems. Nature. 2007;446(7137):782–6.
156. Schulze J, Shibl MF, Al-Marri MJ, Kühn O. Multi-layer multi-configuration time-dependent Hartree (ML-MCTDH) approach to the correlated exciton-vibrational dynamics in the FMO complex. J Chem Phys. 2016;144(18):185101.
157. Moix J, Wu J, Huo P, Coker D, Cao J. Efficient energy transfer in light-harvesting systems, III: the influence of the eighth bacteriochlorophyll on the dynamics and efficiency in FMO. J Phys Chem Lett. 2011;2(24):3045–52.
158. Tronrud DE, Wen J, Gay L, Blankenship RE. The structural basis for the difference in absorbance spectra for the FMO antenna protein from various green sulfur bacteria. Photosynth Res. 2009;100(2):79–87.
159. Nematiaram T, Troisi A. Modeling charge transport in high-mobility molecular semiconductors: balancing electronic structure and quantum dynamics methods with the help of experiments. J Chem Phys. 2020;152(19):190902.
160. Oberhofer H, Reuter K, Blumberger J. Charge transport in molecular materials: an assessment of computational methods. Chem Rev. 2017;117(15):10319–57.
161. Mahan GD. Many-particle physics. Physics of solids and liquids. New York: Springer US; 2000.
162. Prodanović N, Vukmirović N. Charge carrier mobility in systems with local electron–phonon interaction. Phys Rev B. 2019;99(10): 104304.
163. Fratini S, Mayou D, Ciuchi S. The transient localization scenario for charge transport in crystalline organic materials. Adv Funct Mater. 2016;26(14):2292–315.
164. Shuai Z, Peng Q. Organic light-emitting diodes: theoretical understanding of highly efficient materials and development of computational methodology. Natl Sci Rev. 2017;4(2):224–39.
165. Beer M, Longuet-Higgins H. Anomalous light emission of azulene. J Chem Phys. 1955;23(8):1390–1.
166. Itoh T. Fluorescence and phosphorescence from higher excited states of organic molecules. Chem Rev. 2012;112(8):4541–68.
167. Diau EWG, De Feyter S, Zewail AH. Direct observation of the femtosecond nonradiative dynamics of azulene in a molecular beam: the anomalous behavior in the isolated molecule. J Chem Phys. 1999;110(20):9785–8.
168. Shuai Z. Thermal vibration correlation function formalism for molecular excited state decay rates. Chin J Chem. 2020;38(11):1223–32.
169. Humeniuk A, Bužančić M, Hoche J, Cerezo J, Mitrić R, Santoro F, et al. Predicting fluorescence quantum yields for molecules in solution: a critical assessment of the harmonic approximation and the choice of the lineshape function. J Chem Phys. 2020;152(5):054107.

How to cite this article: Ren J, Li W, Jiang T, Wang Y, Shuai Z. Time-dependent density matrix renormalization group method for quantum dynamics in complex systems. WIREs Comput Mol Sci. 2022. e1614. https://doi.org/10.1002/wcms.1614